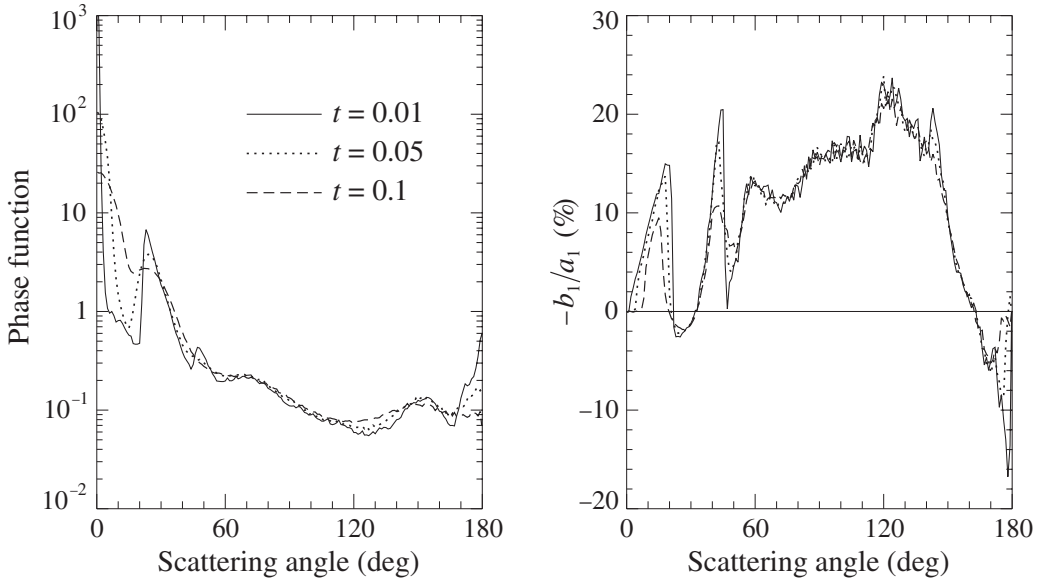

Figure 10.39. The ray-tracing phase function and ratio $-b_1/a_1$ versus scattering angle for randomly oriented hexagonal ice columns with $L/D = 6.2$ and distortion parameters $t = 0.01$, 0.05, and 0.1. The relative refractive index is $m = 1.311$.

microscopic facets that are locally planar and randomly tilted from their orientations corresponding to the case of a smooth surface. The distribution of slopes was assumed to be isotropic and Gaussian with a mean-square surface slope $\sigma^2/2$. Figure 10.40 shows the computation results for randomly oriented clusters composed of nonoverlapping hexagonal ice columns. It is evident that increasing surface roughness strongly affects the scattering properties of ice particles. For the case of smooth crystal surfaces ($\sigma = 0$), the pronounced peaks at $\Theta = 22°, 46°$, and $180°$ as well as the intensity maximum at $\Theta \approx 154°$ are features typical of single hexagonal ice crystals in random orientation (cf. Fig. 10.34). Increasing σ smoothes these features out so that the phase function for $\sigma = 0.1$ consists of a strong diffraction peak and a relatively featureless and flat background. Among the other elements of the scattering matrix, the effect of increasing roughness on the ratio $-b_1/a_1$ appears to be the most significant and makes the scattered polarization largely neutral.

In order to model light scattering by highly irregular polyhedral ice particles, Macke *et al.* (1996b) used a random shape generator based on three-dimensional Koch fractals. The construction of a random Koch fractal is demonstrated in Fig. 10.41. The initial particle (zeroth-generation fractal) is a regular tetrahedron. The first- and second-generation regular Koch fractals are shown in the left-hand column and are obtained via the standard process of self-replication. Progressively disordered versions of these particle are achieved by introducing increasing random displacements of the particle vertices, as shown in the right-hand column. The degree of distortion is defined by the maximum displacement length divided by the length of the crystal segments (as a percentage). Figure 10.42 shows the evolution of the ray-

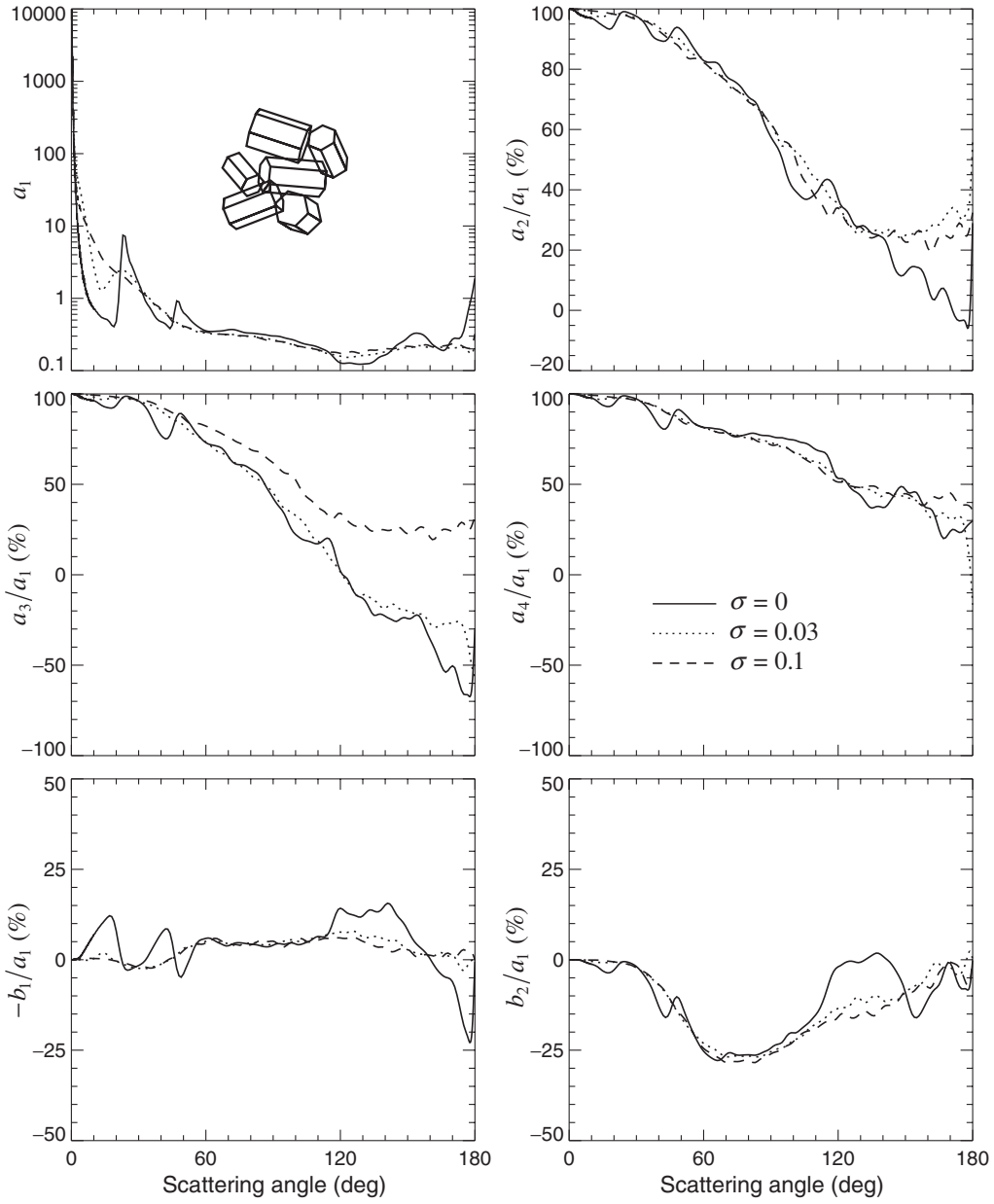

Figure 10.40. Elements of the normalized Stokes scattering matrix versus scattering angle for randomly oriented ice aggregates with smooth ($\sigma = 0$), moderately rough ($\sigma = 0.03$), and deeply rough ($\sigma = 0.1$) surfaces. The maximum dimension of the aggregates is 200 μm, the relative refractive index is 1.311, and the wavelength of light in the surrounding medium is 0.55 μm. (After Yang and Liou 1998a.)

tracing component of the phase function for large, randomly oriented, second-generation ice fractals with increasing distortion. The decrease in direct forward scattering occurs at the expense of an increase in the scattering into adjacent forward-scattering directions. Eventually the phase function becomes almost featureless and approaches a slope at side- and backscattering angles that stays almost constant with a

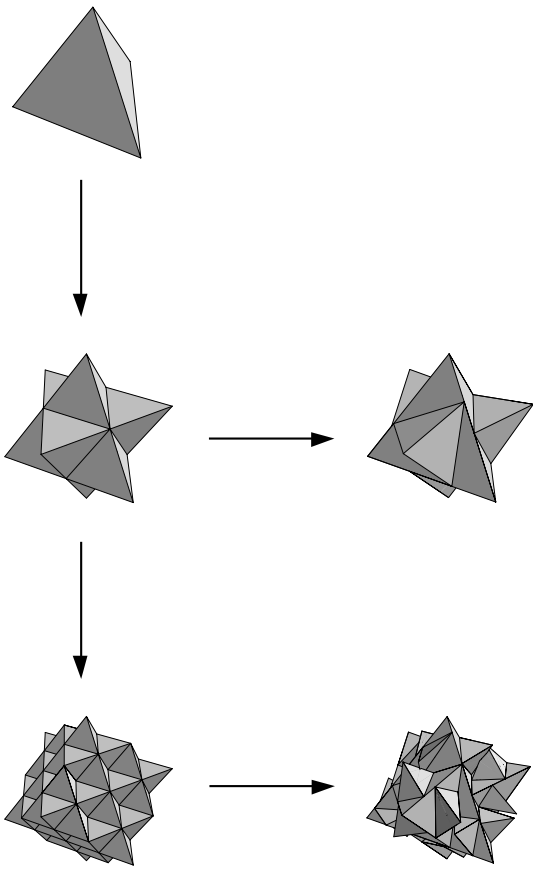

Figure 10.41. Deterministic (left-hand column) and randomized (right-hand column) triadic Koch fractals. Three generations are shown, the zeroth (top) to the second (bottom). (After Macke *et al*. 1996b).

further increase in distortion. This may imply that above a certain level of disorder, the phase function becomes essentially invariant against the particular realization of a random particle shape.

Figure 10.34 contrasts the phase functions computed for randomly oriented hexagonal ice crystals, random second-generation ice fractals with an 18% distortion, and spherical water droplets. The quantitative differences between these phase functions are so large that using an incorrect particle model in retrieval algorithms can seriously affect the results of cloud remote sensing (e.g., Mishchenko *et al.* 1996c; Yang *et al.* 2001b). The corresponding asymmetry parameter differences are relatively smaller: $\langle \cos\Theta \rangle = 0.816$ for the hexagonal ice columns, 0.752 for the random ice fractals, and 0.862 for the water droplets. However, the effect of particle shape on the albedo of

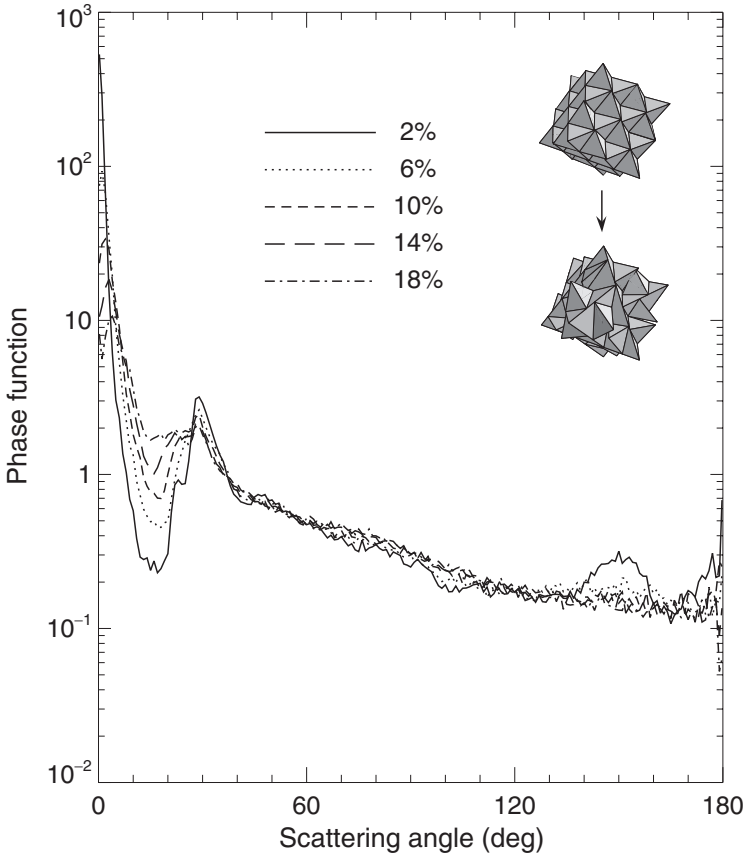

Figure 10.42. Ray-tracing phase function versus scattering angle for randomly oriented second-generation Koch fractals with increasing distortion. The relative refractive index is $m = 1.311$. (After Macke *et al*. 1996b.)

optically thick clouds and the associated radiative forcing of climate can be very strong (e.g., Stephens *et al.* 1990; Mishchenko *et al.* 1996c; Liou *et al.* 2000).

An interesting approach to modeling nearly spherical particles with random rough surfaces was introduced by Muinonen *et al.* (1996). The size and shape of their so-called Gaussian random spheres are specified by the mean and the covariance function of the radius vector. The covariance function is derived from the covariance function of the logarithmic radius, which is expanded in Legendre polynomials. The expansion coefficients are non-negative and provide the spectral weights of the corresponding spherical harmonic components in the Gaussian sphere. The zeroth-degree term controls the overall particle size. The first-degree term is mainly a translation: it moves the particle surface relative to the origin, but the shape itself does not change much. The second-order term produces a deformation with an elongated shape, while higher-degree terms create increasingly complex deformations with larger numbers of protuberances and hollows per solid angle. Increasing the variance of the radius enhances the protuberances and hollows radially. The scattering of light by Gaussian random spheres in the geometrical optics limit has been studied by Muinonen *et al.*

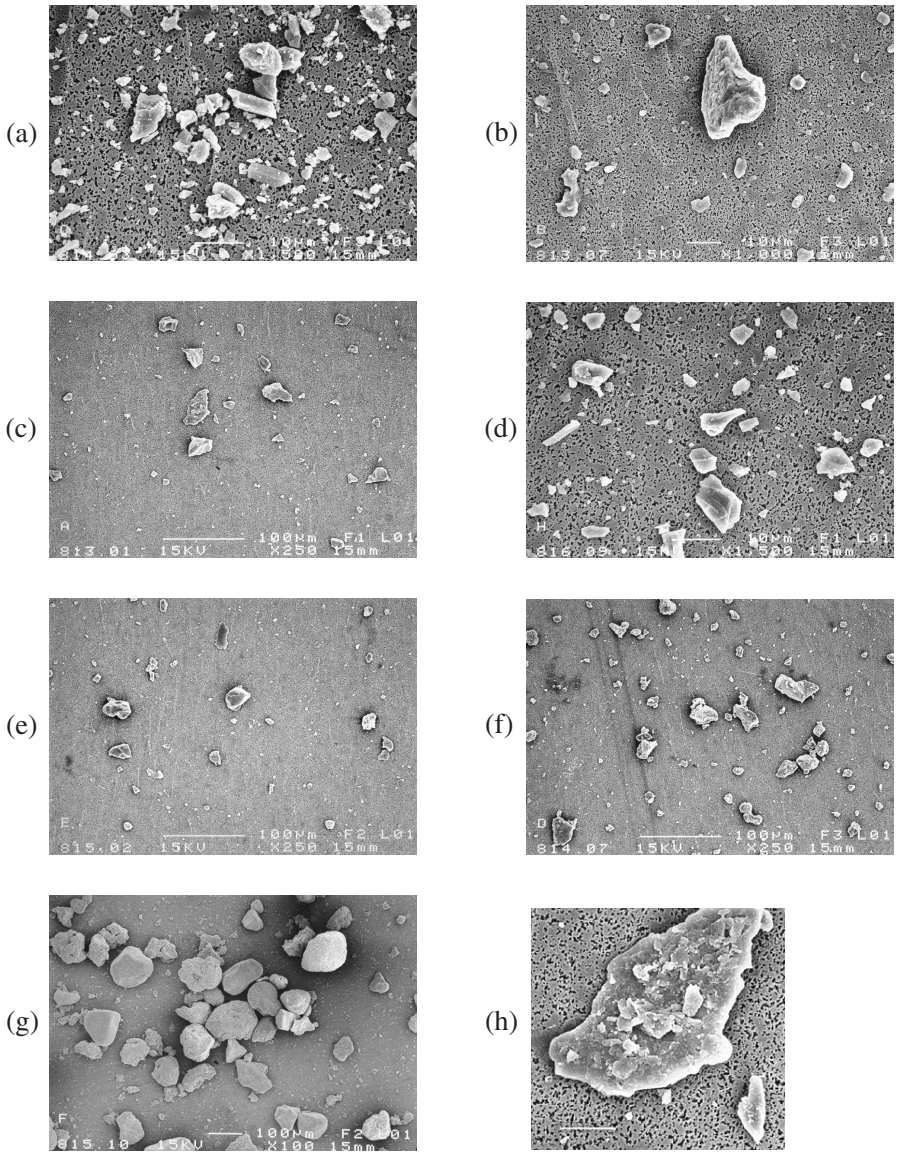

Figure 10.43. Scanning electron microscope images of seven aerosol samples: (a) feldspar, (b) red clay, (c) quartz, (d) Pinatubo volcanic ash, (e) loess, (f) Lokon volcanic ash, and (g) Sahara sand. Panel (h) demonstrates the irregularity of a single quartz particle. The length of the white bars corresponds to 10 μm in panels (a), (b), (d), and (h) and to 100 μm in the remaining panels. (From Volten *et al*. 2001.)

(1996) and Nousiainen and Muinonen (1999) (see also the review by Muinonen 2000).

Despite the recent progress in theoretical modeling, laboratory and *in situ* measurements remain a major source of information about light scattering by irregular particles. Besides the widely acclaimed study by Perry *et al.* (1978), a unique body of experimental data has been collected using the advanced laboratory setup developed at the Free University in Amsterdam (Kuik *et al.* 1991; Kuik 1992; Volten *et al.* 1998,

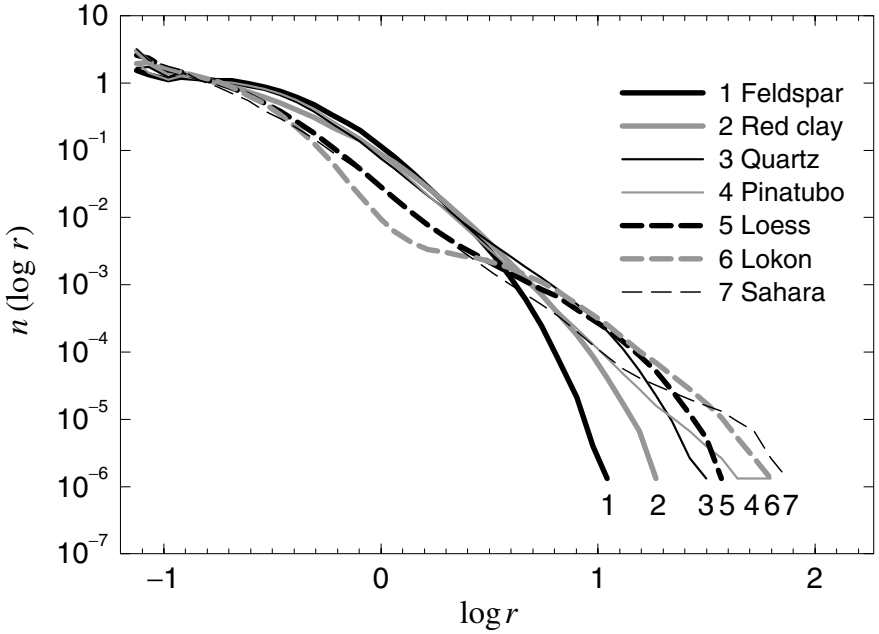

Figure 10.44. Measured normalized size distributions $n(\log r) = rn(r)\ln 10$ of the projected-area-equivalent-sphere radius r for the seven aerosol samples shown in Fig. 10.43. (From Volten *et al.* 2001.)

1999, 2001; Vermeulen 1999; Hovenier 2000; Muñoz *et al.* 2000a, b, 2001; Volten 2001). For example, Fig. 10.43 shows microphotographs of seven mineral aerosol samples studied by Volten *et al.* (2001), while Fig. 10.44 depicts the respective normalized distributions of projected-area-equivalent-sphere radii (in micrometers). It is evident that all particles studied have irregular and strongly variable compact shapes. Table 10.4 provides a brief characterization of the samples including the corresponding effective radii and approximate ranges of the real part of the relative refractive index based on the literature values for the main constituent minerals. The results of measurements at the wavelengths 632.8 and 441.6 nm are shown in Figs. 10.45–10.51. The phase functions are normalized to unity at $\Theta = 30°$. Other elements of the normalized Stokes scattering matrix are shown relative to the corresponding phase function. The measurements were taken at $5°$ intervals for Θ in the range from $5°$ to $170°$ and at $1°$ intervals for Θ from $170°$ to $173°$. Scattering matrix elements other than those shown in these figures were found to be zero within the error bars, which was a good indication that the particles formed a macroscopically isotropic and mirror-symmetric scattering medium.

The phase functions for all samples studied are smooth functions of the scattering angle and exhibit a steep forward peak and essentially no structure at side- and backscattering angles. Most of the phase-function curves are remarkably shallow at side-scattering angles (cf. Perry *et al.* 1978; Nakajima *et al.* 1989; Muñoz *et al.* 2000a) and do not show the deep side-scattering minimum typical of spherical particles, caused

Table 10.4. Characteristics of seven mineral particle samples studied by Volten *et al.* (2001)

Sample	Composition	r_{eff} (μm)	m_{R}	Color
Feldspar	K-feldspar, plagioclase, quartz	1.0	1.5–1.6	light pink
Red clay	biotite, illite, quartz	1.5	1.5–1.7	red brown
Quartz	quartz	2.3	1.54	white
Pinatubo volcanic ash	glass, plagioclase, amphibole, magnetite	3.0	1.5–1.7 2.1	light gray
Loess	K-feldspar, illite, quartz, calcite, chlorite, albite	3.9	1.5–1.7	yellow brown
Lokon volcanic ash	silica glass, plagioclase, magnetite	7.1	1.5–1.6 2.1	dark brown
Sahara sand	quartz, clay minerals, calcium carbonate	8.2	1.5–1.7	yellow brown

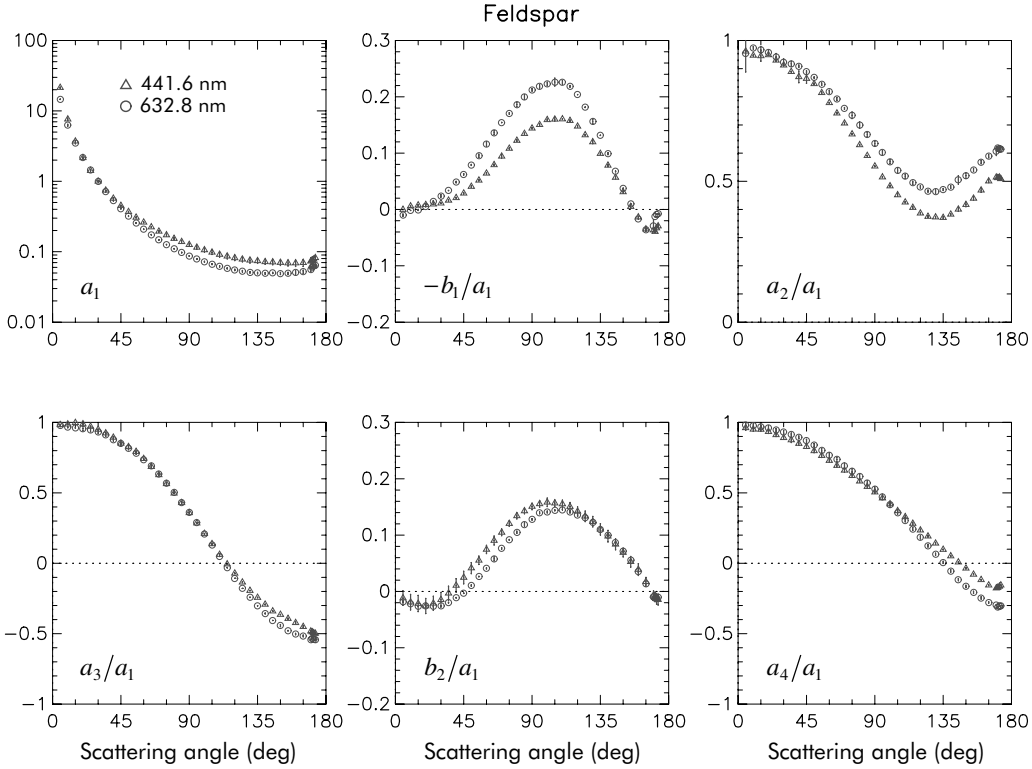

Figure 10.45. The phase function a_1 and the scattering matrix element ratios $-b_1/a_1$, a_2/a_1, a_3/a_1, b_2/a_1, and a_4/a_1 versus scattering angle Θ for feldspar. The circles and triangles denote measurements at wavelengths 632.8 and 441.6 nm, respectively, together with their error bars. The phase functions are normalized to unity at $\Theta = 30°$. The sign of the ratio b_2/a_1 is opposite to that adopted elsewhere in this book. (From Volten *et al*. 2001.)

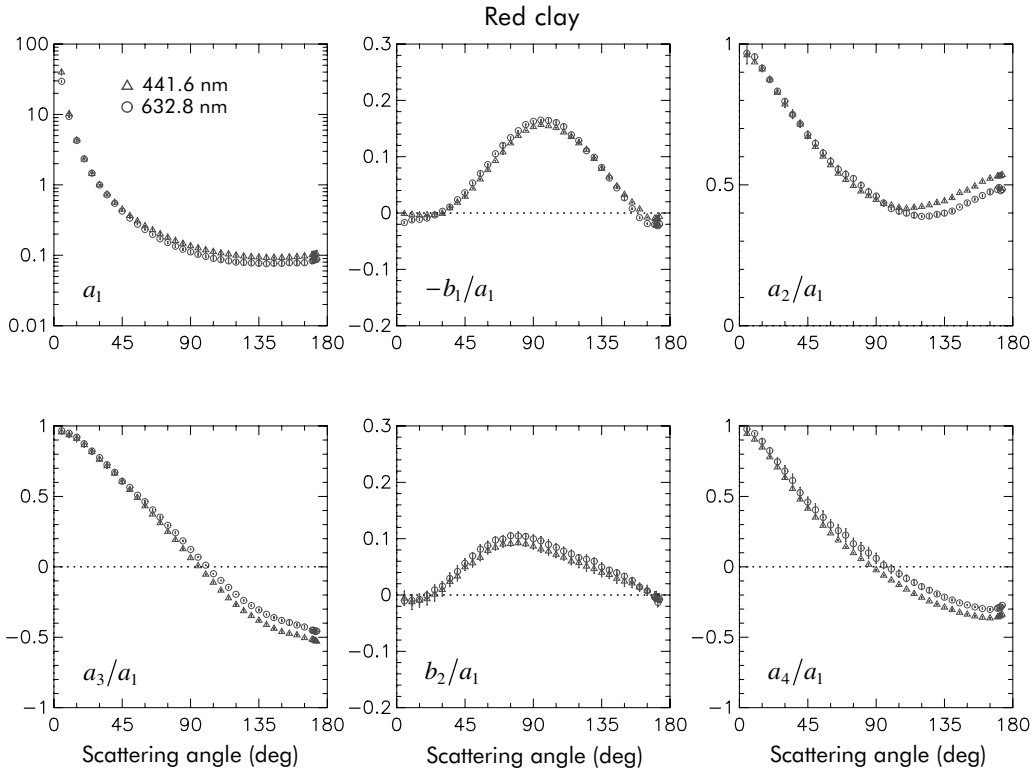

Figure 10.46. As in Fig. 10.45, but for red clay (from Volten *et al*. 2001).

by the Alexander's dark band lying between the primary and secondary rainbows (cf. Fig. 7.4 and Section 9.4). Some of the phase-function curves seem to show the beginning of a backscattering enhancement, but the lack of measurements for $\Theta > 173°$ makes this observation inconclusive. The curves for the ratio $-b_1/a_1$ are also similar for all samples and display a broad positive maximum at side-scattering angles and a weak and narrow negative branch at backscattering angles. The curves for the ratio a_2/a_1 are remarkably similar as well and deviate significantly from unity at side- and backscattering angles: they descend from almost unity at small scattering angles to a minimum at scattering angles close to $120°-130°$ and then increase again as Θ approaches 180°. The depth of the minimum appears to be size dependent and increases as the effective radius grows from 1.0 μm for feldspar to 8.2 μm for Sahara sand. The curves for the ratios a_3/a_1 and a_4/a_1 are largely featureless and deviate significantly from –1 at backscattering angles. The ratio a_4/a_1 is always larger than the ratio a_3/a_1 in the backward hemisphere. Volten *et al.* (2001) use the time factor $\exp(\mathrm{i}\omega t)$ rather than $\exp(-\mathrm{i}\omega t)$ to define the Stokes parameters, which causes a sign change in the numerical values of the ratio b_2/a_1 (cf. Mishchenko *et al.* 2000b). Therefore, in terms of the time-factor convention adopted in this book, the results of Volten *et al.* show that this ratio typically has weak positive branches at small and large scattering angles separated by a wide range of negative values. Most of these observations are in qualitative agreement with the conclusions derived from the *T*-

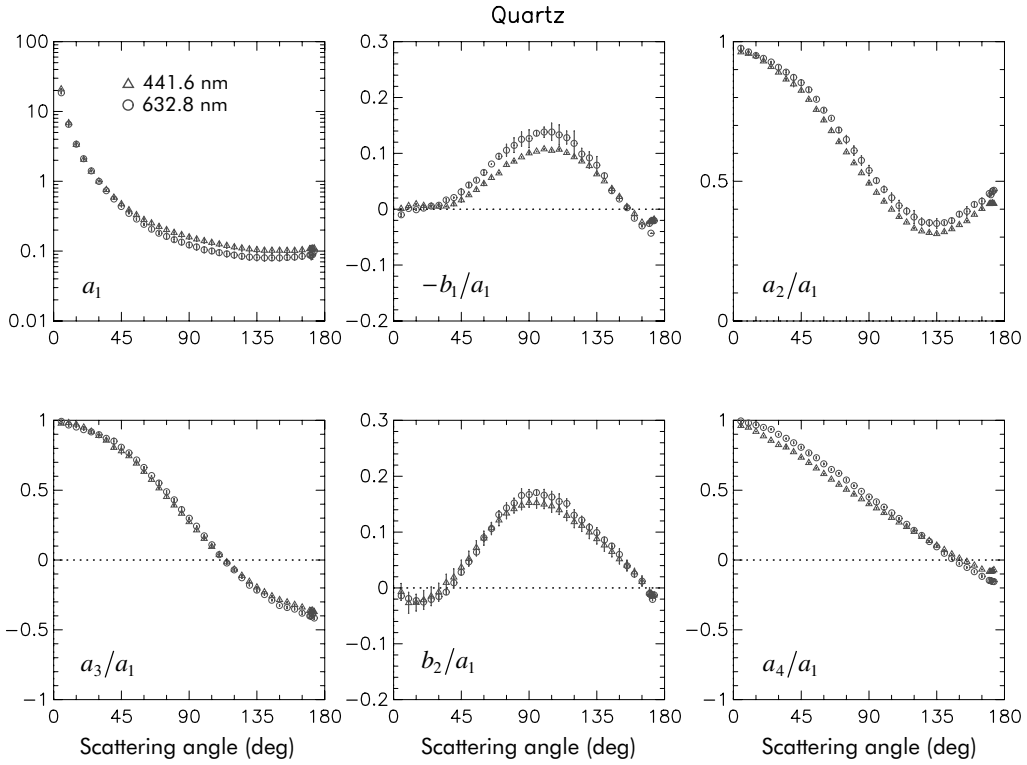

Figure 10.47. As in Fig. 10.45, but for quartz (from Volten *et al*. 2001).

matrix results for moderately aspherical polydisperse spheroids and cylinders as discussed in Sections 10.2 and 10.3.

The similarity of the laboratory results for the different mineral-particle samples prompted Volten *et al.* (2001) to construct an average scattering matrix for use in qualitative or semi-quantitative analyses of remote sensing observations or laboratory and *in situ* measurements, especially in those cases when the specific microphysical characteristics of mineral particles are not known *a priori*. The average phase function was calculated by averaging the 14 phase functions measured at both wavelengths. Since no scattering cross sections were available, the experimental phase functions were averaged by giving them equal weights. Therefore, the normalization to unity at $\Theta = 30°$ also holds for the average phase function. Each measured element ratio was multiplied by the normalized phase function measured for the particular sample and wavelength, thereby yielding elements instead of element ratios. Finally, each element was averaged over the respective 14 measurements and divided by the average phase function. The resulting average phase function and element ratios are depicted in Fig. 10.52. For comparison, this figure also shows the bands of sample variability, defined as the areas between the highest and lowest measured values in Figs. 10.45–10.51 not taking into account the error bars for the individual measurements. The laboratory data displayed in Figs. (10.45)–(10.52) were presented by Volten (2001) in tabular form and will undoubtedly prove very useful in future

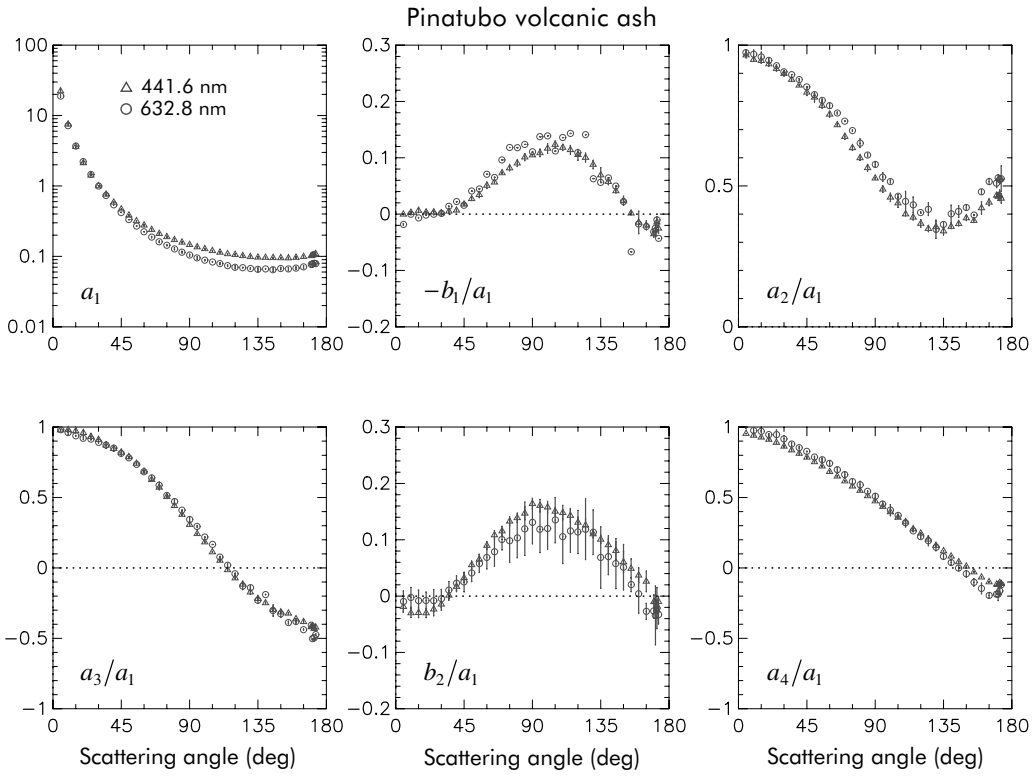

Figure 10.48. As in Fig. 10.45, but for Pinatubo volcanic ash (from Volten *et al*. 2001).

analyses of light scattering by irregular particles. For example, the laboratory data for green clay particles with an effective radius of 1.55 μm (Muñoz *et al.* 2000b) generally agree with the overall trends exhibited by the average scattering matrix elements and fall within the bands of sample variability (Fig 10.53). This comparison suggests that the average model derived by Volten *et al.* (2001) may indeed be representative of ensembles of irregular, compact mineral particles with sizes comparable to and larger than a wavelength.

10.8 Statistical approach

Since theoretical computations for irregular particles with sizes comparable to the wavelength remain problematic, several attempts have been made to model the scattering and absorption properties of irregular particles using simple, regular shapes. These attempts are based on the realization that in addition to size and orientation averaging, as discussed in Section 10.1, averaging over shapes may also prove to be necessary in many cases. More often than not, natural and artificial particle samples exhibit a great variety of shapes, thereby making questionable the ability of a single nonspherical shape to represent scattering properties of a shape mixture. We have

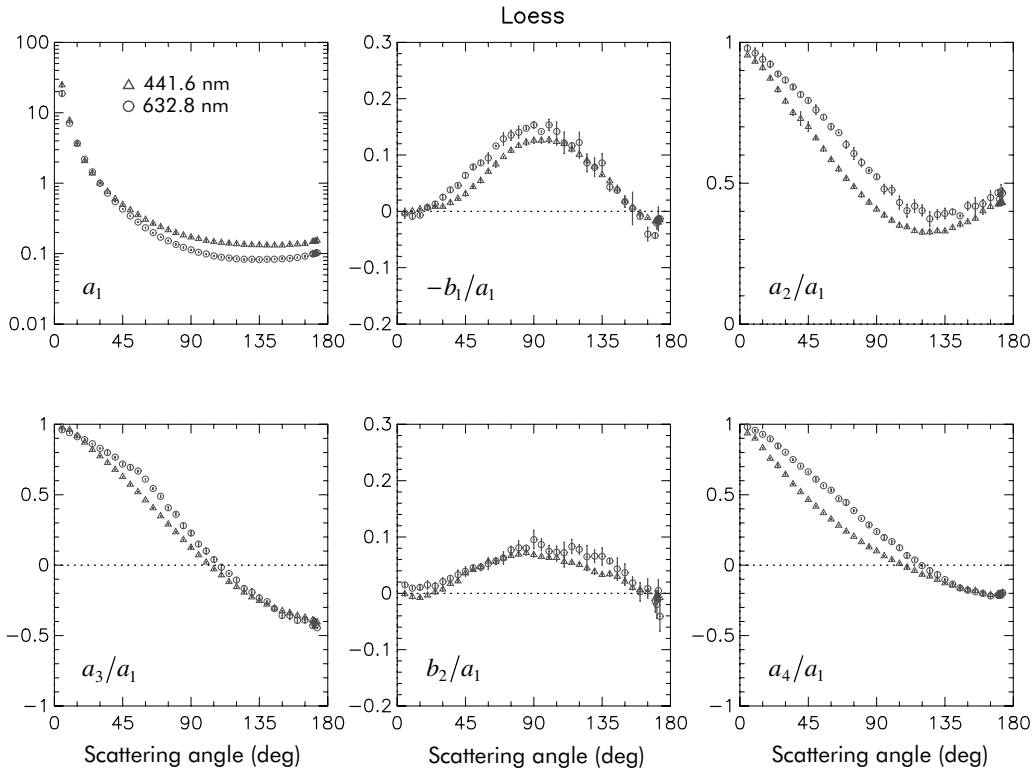

Figure 10.49. As in Fig. 10.45, but for loess (from Volten *et al*. 2001).

seen, indeed, that even after size and orientation averaging, essentially any deterministic particle shape produces a unique, shape-specific scattering pattern, whereas experimental measurements for real nonspherical particles usually show smooth, featureless patterns. As an example, Plate 10.7(a) depicts the phase function for a monodisperse sphere with radius 1.163 μm and surface-equivalent, monodisperse, randomly oriented prolate spheroids with aspect ratios ε increasing from 1.2 to 2.4. The wavelength of the light in the surrounding medium is 0.443 μm, and the relative refractive index is 1.53 + i0.008. Whereas the monodisperse curves form a tangle of lines with no clear message, averaging over sizes, as shown in Plate 10.7(b), makes the phase functions much smoother and reveals a systematic change with increasing aspect ratio that renders each phase-function curve unique and dissimilar to all other curves. However, this uniqueness is suppressed and ultimately removed by averaging over an increasingly wide aspect-ratio distribution of prolate spheroids, centered on $\varepsilon = 1.8$, Plate 10.7(c), and by a subsequent mixing of prolate and oblate spheroids, Plate 10.7(d). The resulting phase function (the red curve in Plate 10.7(d)) is very smooth and featureless and, in fact, almost perfectly coincides with the phase function experimentally measured by Jaggard *et al.* (1981) for micrometer-sized, irregularly shaped soil particles (cf. Fig. 10.54). Both phase functions show the typical en-

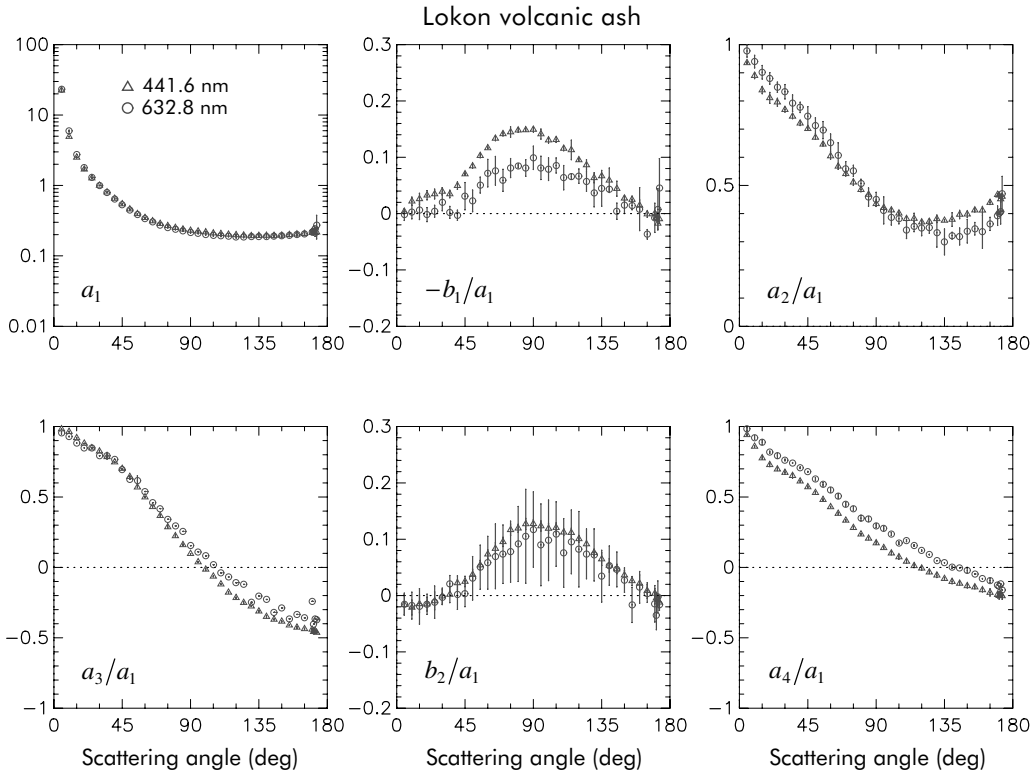

Figure 10.50. As in Fig. 10.45, but for Locon volcanic ash (from Volten *et al*. 2001).

hancement of side scattering and suppression of backscattering relative to the phase function for surface-equivalent spheres.

This example may have two important implications. First, it may indicate that the often observed smooth scattering-angle dependence of the elements of the scattering matrix for samples of natural and artificial nonspherical particles is largely caused by the diversity of particle shapes in the samples. Second, it may suggest that at least some scattering properties of ensembles of irregular particles can be adequately modeled using a polydisperse shape mixture of simple particles such as spheroids. The assumptions that particles chosen for the purposes of ensemble averaging need not be in one-to-one correspondence with the ensemble of irregular particles of interest and that they may have relatively simple shapes are central to the so-called statistical approach (Shifrin and Mikulinsky 1987; Mugnai and Wiscombe 1989; Bohren and Singham 1991). The need for this kind of approach stems from the fact that it is often impossible to specify exactly the shapes and sizes of all particles forming a natural or artificial sample. Even if it were possible, the low efficiency of the exact numerical techniques applicable to arbitrarily shaped particles would entail a prohibitively expensive computational effort. However, the availability of techniques like the *T*-matrix method, which is very fast for randomly oriented, rotationally symmetric particles and is applicable to large size parameters, makes the statistical approach feasible. Applications of this approach by Bohren and

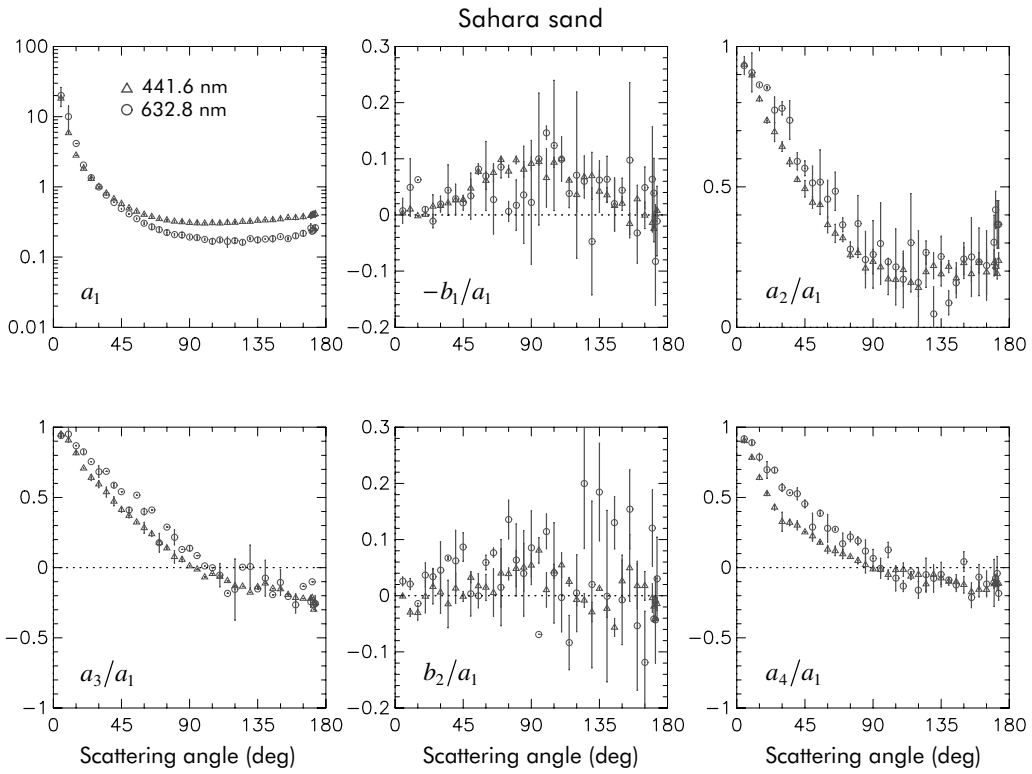

Figure 10.51. As in Fig. 10.45, but for Sahara sand (from Volten *et al*. 2001).

Huffman (1983, Chapter 12), Nevitt and Bohren (1984), Hill *et al.* (1984), Mishchenko *et al.* (1997a), and Goncharenko *et al.* (1999) suggest that it may indeed be a valuable practical tool in many cases.

10.9 Clusters of spheres

The scattering and absorption properties of simple two-sphere clusters (bispheres) have been extensively studied by Mishchenko *et al.* (1995) using the superposition *T*-matrix method. Panels (b) and (c) of Plate 10.8 depict the degree of linear polarization for scattering of unpolarized incident light, i.e., the ratio

$$-\frac{Z_{21}(\vartheta^{\rm sca}, \varphi^{\rm sca}=0; \vartheta^{\rm inc}=0, \varphi^{\rm inc}=0)}{Z_{11}(\vartheta^{\rm sca}, \varphi^{\rm sca}=0; \vartheta^{\rm inc}=0, \varphi^{\rm inc}=0)},$$

as a function of the zenith angle of the scattering direction and the monodisperse constituent-sphere size parameter for two orientations of the bisphere axis with respect to the laboratory reference frame. The bispheres have identical touching components, and the bisphere axis is defined as the line connecting the constituent-sphere centers. These plots show that the bisphere polarization is strongly dependent on the particle

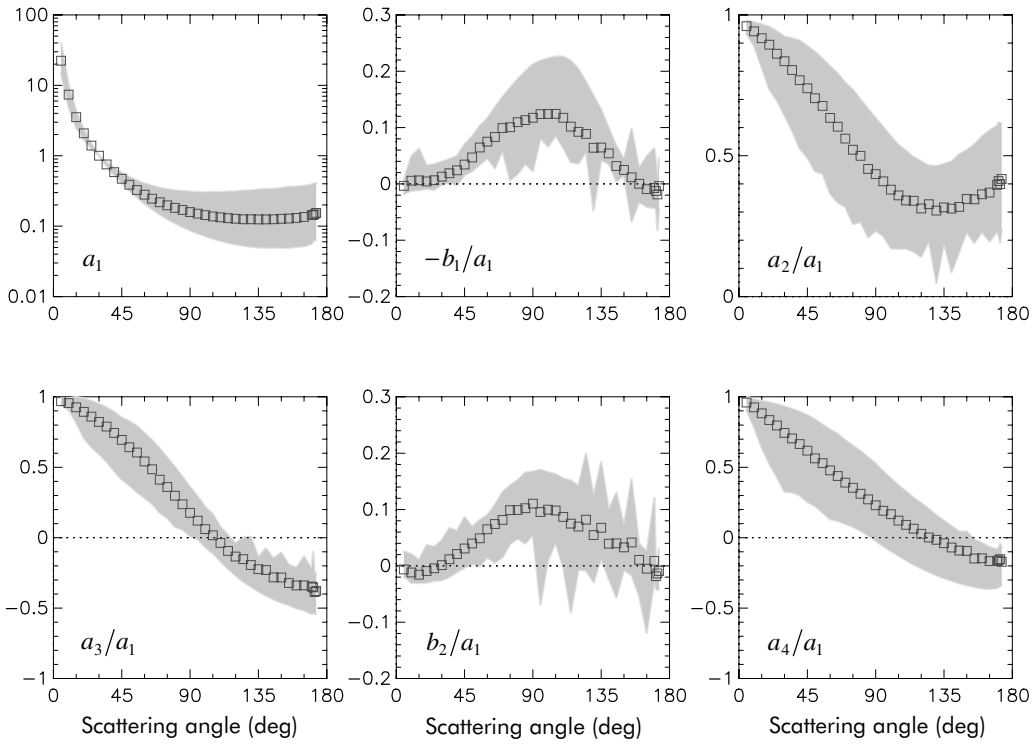

Figure 10.52. The squares show the average phase function a_1 (normalized to unity at $\Theta = 30°$) and the scattering matrix element ratios $-b_1/a_1$, a_2/a_1, a_3/a_1, b_2/a_1, and a_4/a_1 versus scattering angle Θ. The gray bands indicate the domains spanned by the measurements for individual particle samples. The sign of the ratio b_2/a_1 is opposite to that adopted elsewhere in this book. (From Volten *et al*. 2001.)

orientation and reveals a much more complicated structure than the single-sphere polarization pattern shown in Plate 10.8(a). In particular, the lack of axial symmetry for the scattering geometry in Plate 10.8(c) makes the linear polarization non-zero at $\vartheta^{\rm sca} = 0°$ and, more noticeably, at $\vartheta^{\rm sca} = 180°$. Also, the number of local maxima and minima has increased sharply. This means that in addition to the single-sphere resonant structure the bispheres exhibit a significant contribution due to the cooperative scattering of light from the two constituent spheres.

Plate 10.8(d) shows the calculation results for monodisperse bispheres in random orientation. Somewhat unexpectedly, we see a polarization pattern that is strikingly similar to that of single monodisperse spheres, Plate 10.8(a). The only obvious difference is that the amplitudes of the local maxima and minima are reduced, although their locations and numbers are exactly the same. This means that averaging over bisphere orientations largely cancels the cooperative scattering contribution and slightly blurs the single-sphere resonant structure. This result is well illustrated by Fig. 10.55, which shows the elements of the normalized Stokes scattering matrix for a randomly oriented two-sphere cluster with identical touching components, together with those for a single sphere with size parameter equal to that of the cluster compo-

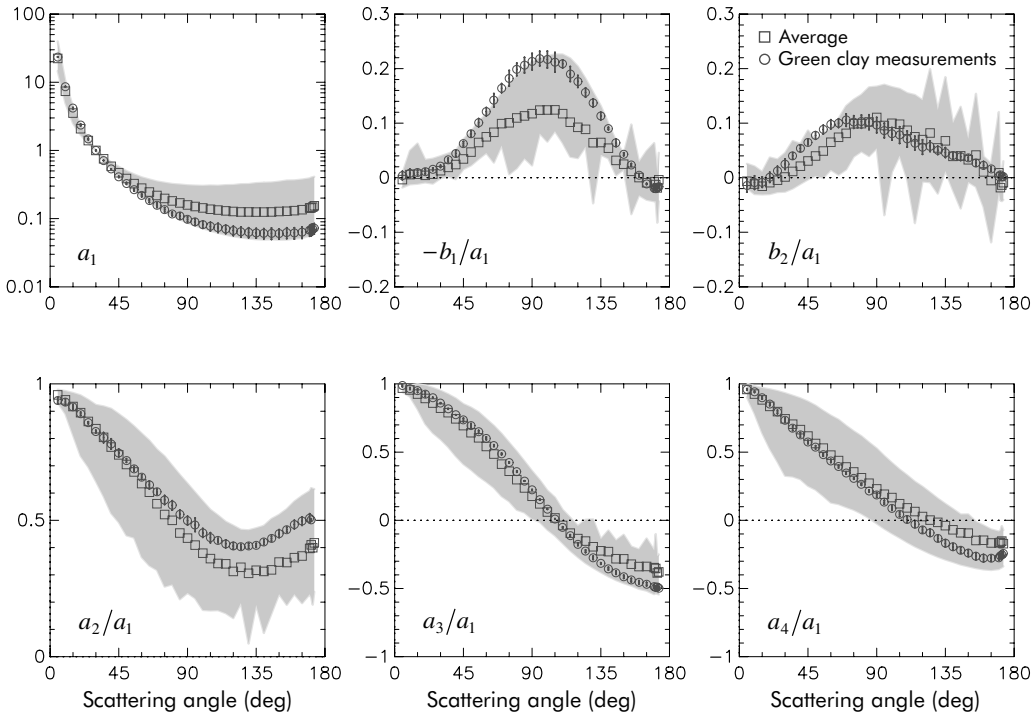

Figure 10.53. The circles depict the measured phase function a_1 and scattering matrix element ratios $-b_1/a_1$, b_2/a_1, a_2/a_1, a_3/a_1, and a_4/a_1 versus scattering angle for green clay particles at a wavelength 633 nm (from Muñoz *et al.* 2000b). The squares and the gray bands indicate the average scattering matrix and the domains spanned by the measurements for seven mineral particle samples (Volten *et al.* 2001).

nents for comparison. It is obvious that the dominant feature in the cluster scattering is the single scattering from the component spheres, albeit diminished by orientation averaging. The only distinct manifestations of the fact that the bisphere is a nonspherical particle are the departure of the ratio a_2/a_1 from unity and the detectable lack of equality of the elements a_3 and a_4. These two effects are especially noticeable at backscattering angles and are further illustrated in Fig. 10.56, which shows the linear and circular depolarization ratios for randomly oriented bispheres with touching components as a function of the component-sphere size parameter. Both depolarization ratios vanish in the limit of zero size parameter, but become appreciable for $x \gtrsim 1$ and reach especially large values at size parameters from about 15 to 20.

Figures 10.57 and 10.58 show ratios of bisphere and single-sphere quantities: the optical cross sections, the single-scattering albedo, and the asymmetry parameter. The bispheres are randomly oriented and the size of the single sphere is equal to the size of each bisphere component. Interestingly, all these ratios are nearly constant at size parameters exceeding 15. The ratio of the extinction cross sections (the solid curve in Fig. 10.57) shows both high-frequency ripple and low-frequency oscillations. However, the amplitude of the oscillations is small, and the entire curve for size parameters exceeding

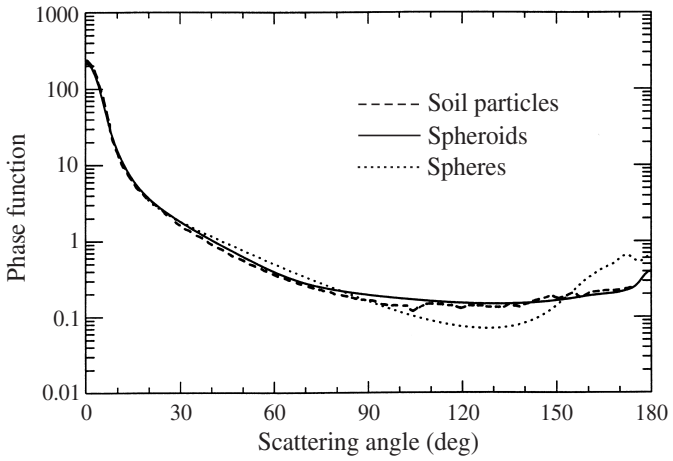

Figure 10.54. Phase functions measured by Jaggard *et al.* (1981) for natural wavelength-sized soil particles and computed for a broad shape distribution of polydisperse, randomly oriented spheroids and surface-equivalent spheres.

6 is close to 1.8–1.85. The ratio of the orientation-averaged geometrical cross section of a bisphere to the geometrical cross section of a sphere with size equal to that of each bisphere component is 1.849. Therefore, in the geometrical optics limit the ratio of the bisphere and single-sphere extinction cross sections must be equal to this value, 1.849. It can be seen that the extinction ratio curve shows a distinct trend toward this limit with increasing size parameter. However, it is interesting that the extinction ratio is close to the geometrical optics limit for size parameters as small as 7.

Despite a small-amplitude high-frequency ripple, the ratio of the absorption cross sections (the broken-and-dotted curve in Fig. 10.57) is close to 2 for the entire range of size parameters shown, thus indicating that the absorption cross section is roughly proportional to the particle volume. However, if the imaginary part of the relative refractive index is non-zero then in the limit of infinite size parameter all light refracted into the particle is absorbed and does not escape. Therefore we should expect that the ratio of the absorption cross sections should decrease with increasing size parameter and approach the geometrical cross section ratio of 1.849, as seen indeed in Fig. 10.57. The scattering cross section ratio (the dotted curve in Fig. 10.57) closely follows the extinction cross section ratio except at size parameters smaller than unity, where extinction is dominated by absorption.

The single-scattering albedo ratio (the dotted curve in Fig. 10.58) is especially size-parameter independent for size parameters greater than unity and varies within a very narrow range, 1 ± 0.02. The asymmetry parameter ratio (the solid curve in Fig. 10.58) is also close to unity. However, all these ratios, except for the absorption cross section ratio, rise substantially as the size parameter becomes smaller than 2, which demonstrates the increasing influence of cooperative scattering effects for smaller particles.

As we have seen previously, one of the main effects of averaging scattering

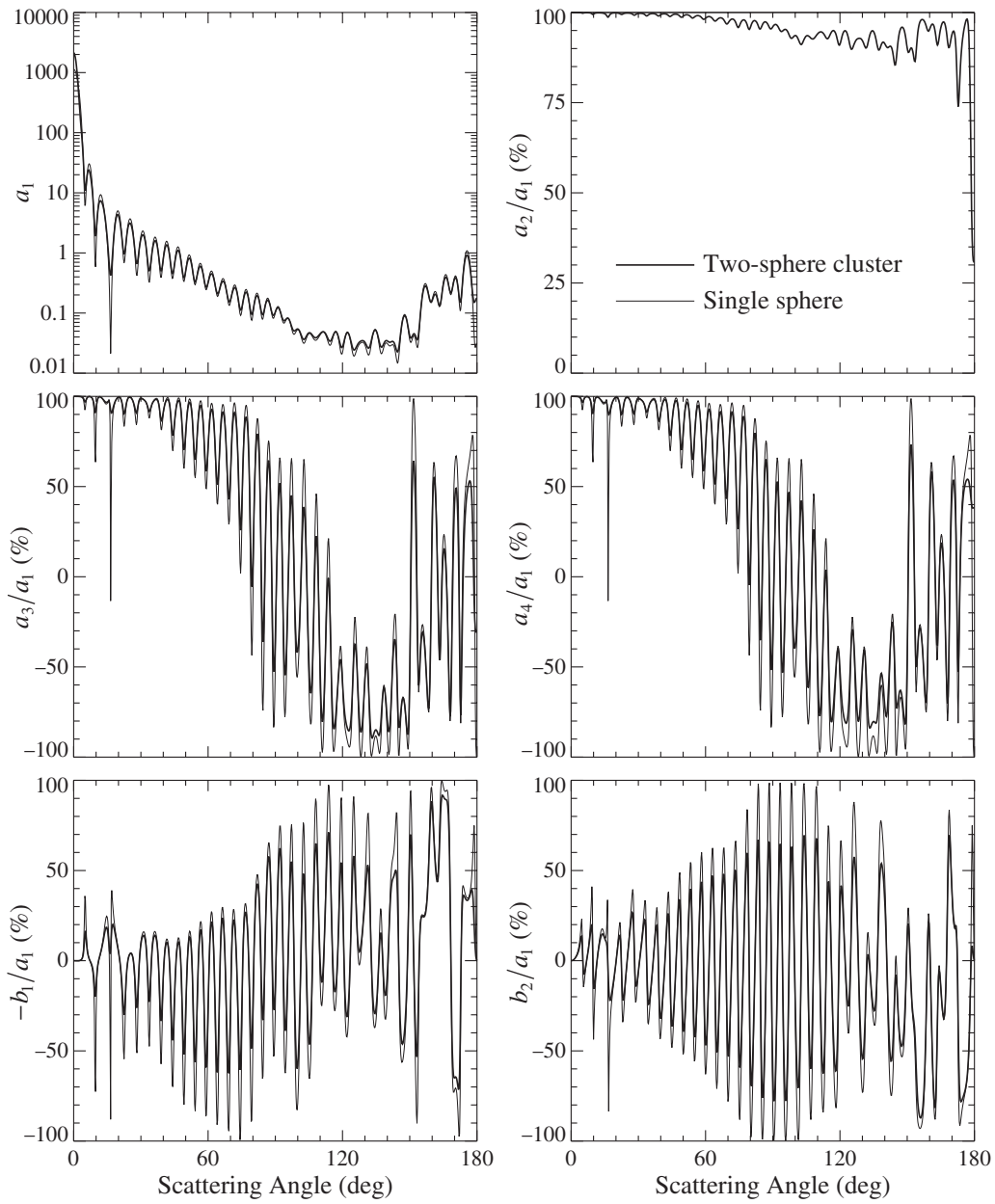

Figure 10.55. Scattering matrix elements for a randomly oriented two-sphere cluster with touching components and a single sphere. The component spheres and the single sphere have the same size parameter 40 and the same relative refractive index 1.5 + i0.005.

characteristics over a size distribution is to wash out the resonance structure typical of monodisperse particles. This effect facilitates comparisons of light-scattering properties of particles with different shapes and is illustrated in Fig. 10.59, which shows the elements of the normalized Stokes scattering matrix for power law size distributions of spheres and of randomly oriented bispheres. This figure demonstrates again that the angular dependence of the elements of the scattering matrix for bispheres is similar to that for single spheres with effective size parameter equal to the effective

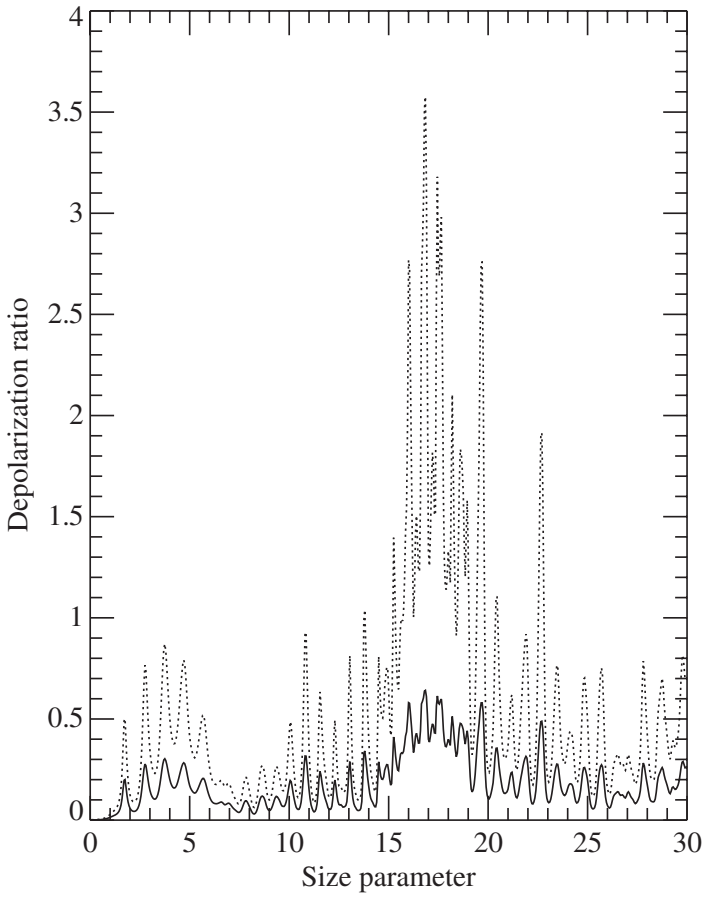

Figure 10.56. Linear (solid curve) and circular (dotted curve) backscattering depolarization ratios versus constituent-sphere size parameter for randomly oriented monodisperse bispheres with equal touching components and a relative refractive index 1.5 + i0.005.

bisphere monomer size parameter. The ratios $-b_1/a_1$ and b_2/a_1 for the bispheres and the single spheres are especially similar. The phase functions a_1 are also close to one another except at scattering angles smaller than 10°, where the bisphere intensity is nearly twice that for single spheres because of the constructive interference of light singly scattered by bisphere components in the exact forward direction (Mishchenko 1996a). Again, the only unequivocal indications of particle nonsphericity for bispheres are the differences between the ratios a_3/a_1 and a_4/a_1 and the departure of the ratio a_2/a_1 from unity. For comparison, Fig. 10.59 also depicts the scattering matrix elements for polydisperse, randomly oriented prolate spheroids with aspect ratio 2 and effective volume-equivalent-sphere size parameter 10. It is seen that, unlike the case for the spheres and the bispheres, the spheroid phase function exhibits enhanced side scattering and suppressed backscattering, while the degree of linear polarization is positive at scattering angles around 120°. The differences between the ratios a_2/a_1, a_3/a_1, a_4/a_1, and b_2/a_1 for the spheres and the spheroids are also greater than those for the spheres and the bispheres.

Figures 10.60 and 10.61 depict the scattering matrix elements for two distinctly

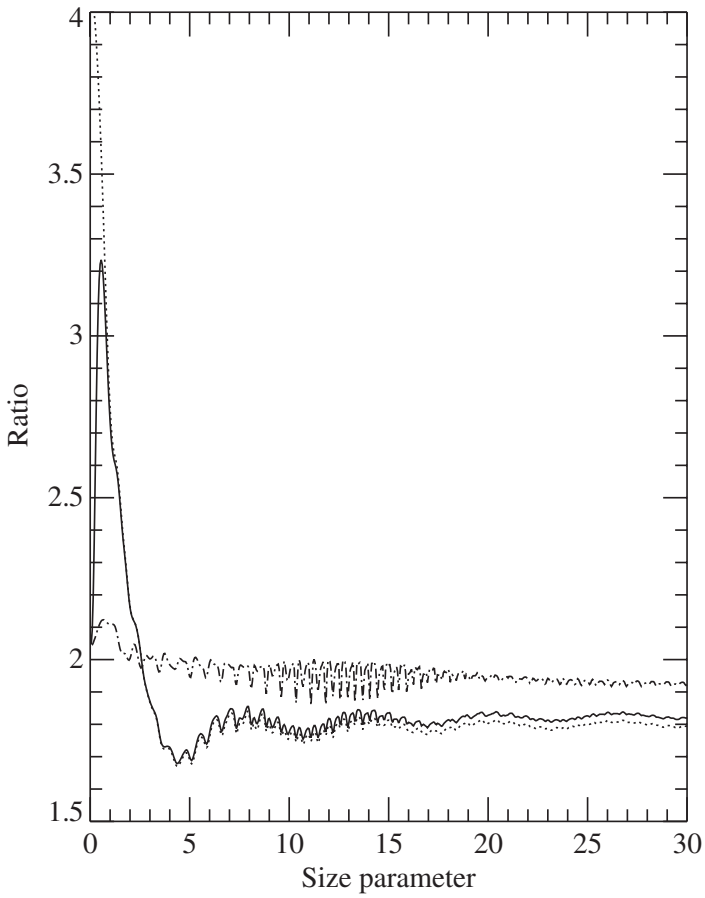

Figure 10.57. Ratios of extinction (solid curve), scattering (dotted curve), and absorption (broken-and-dotted curve) cross sections for monodisperse randomly oriented bispheres with equal touching components and for monodisperse single spheres, versus single-sphere size parameter. For bispheres, the horizontal axis shows the values of the constituent-sphere size parameter. The relative refractive index is 1.5 + i0.005.

different types of sphere cluster, each with N_s identical wavelength-sized components, for $N_s = 1, 2, 3, 4,$ or 5. In Fig. 10.60 the cluster is a straight chain whereas in Fig. 10.61 the spheres are packed into a tetrahedral lattice. These two types of clusters represent extrema in the packing density of touching spheres. A quick inspection of the figures reveals that the configuration of the component spheres can have a significant effect on the cluster scattering properties. Aside from the increase in the forward-scattering value of the phase function caused by the constructive interference of the light singly scattered by the cluster components in the exact forward direction, the matrix elements for the straight chain (Fig. 10.60) attain a form that is nearly independent of N_s for $N_s \geq 2$. As for bispheres, clustering results in a damping of the oscillations in the matrix elements compared with those for a single sphere, yet the locations of the maxima and minima for the chain are essentially the same as those for the single-sphere case. The obvious exception is the ratio a_2/a_1, which is identically unity for the sphere. However, the matrix elements for the densely packed cluster

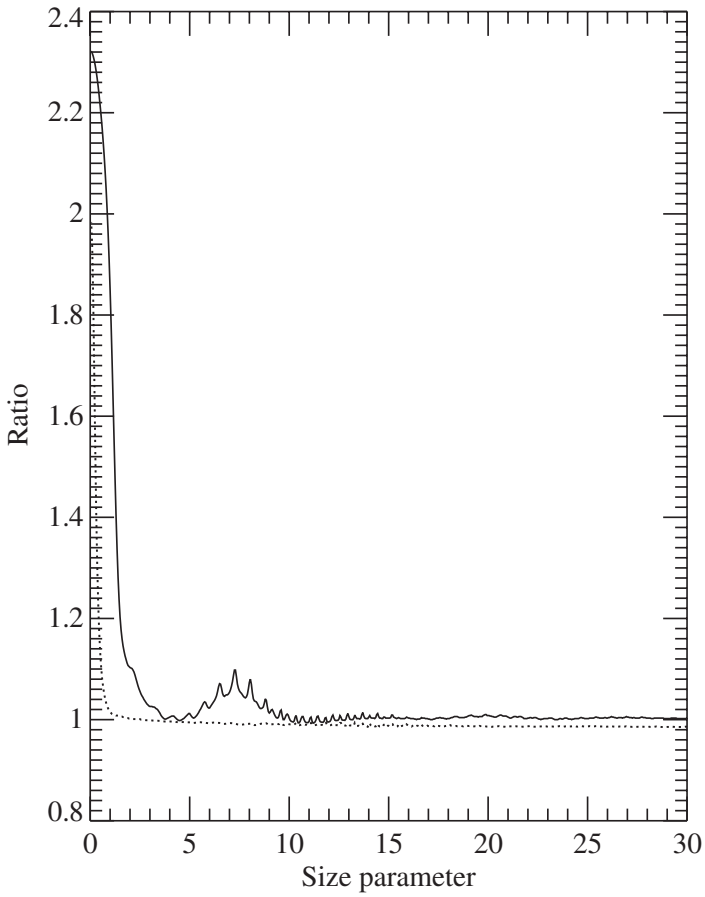

Figure 10.58. As in Fig. 10.57, but for the ratios of the single-scattering albedos (dotted curve) and of the asymmetry parameters (solid curve).

change significantly with increasing N_s and appear to approach a saturation level in which all oscillations eventually vanish. The effect of packing density is especially noticeable in the backward-direction values of the ratios a_2/a_1, a_3/a_1, and a_4/a_1 and, thus, in increased linear and circular depolarization ratios.

To explain the differences in the scattering patterns for these two types of cluster configuration, we first note that the two major effects of aggregation on scattering are interference of the fields scattered by the cluster components in the far-field zone and multiple internal scattering among the components. When the size parameters of the spheres are of order unity or greater (as is the case for Figs. 10.60 and 10.61), averaging over a uniform orientation distribution acts to zero out the effect of interference in all directions but the exact forward direction. The differences between the single-sphere and orientation-averaged cluster scattering patterns are therefore caused mostly by multiple scattering. Multiple scattering for the linear chain configuration occurs primarily between neighboring spheres, and because of this the scattering matrix elements for $N_s \geq 3$ do not differ much from those of the bisphere – except for the phase function at $\Theta = 0°$. However, the packed-cluster configuration offers a

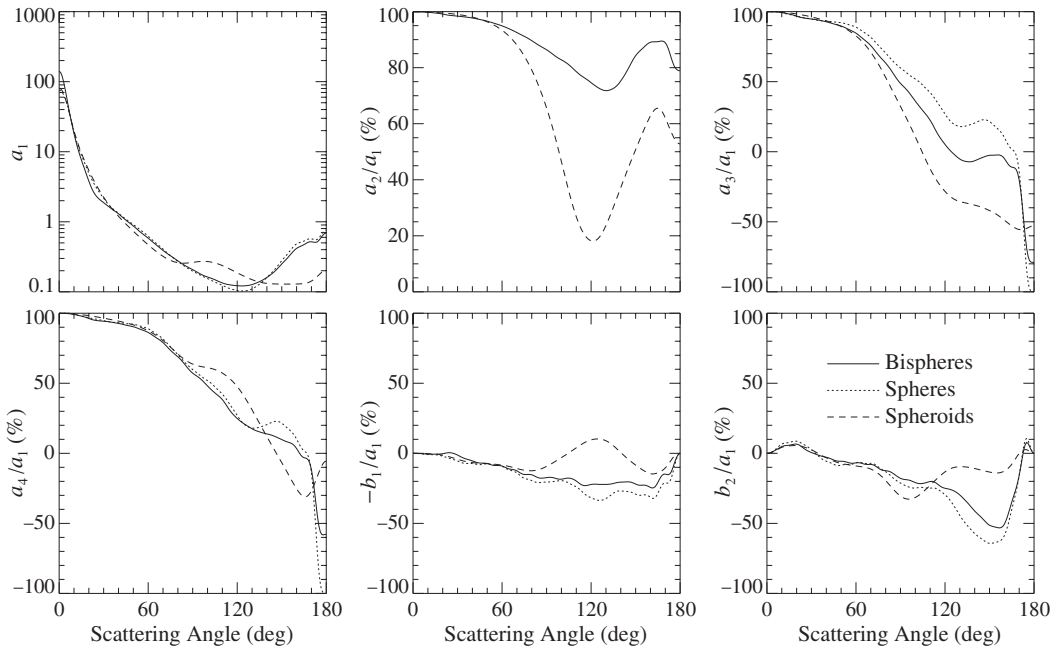

Figure 10.59. Elements of the normalized Stokes scattering matrix for polydisperse randomly oriented bispheres with equal touching components and effective constituent-sphere size parameter $x_{\rm eff} = 10$ and for polydisperse single spheres with the same effective size parameter. For comparison, the figure also shows the results for polydisperse, randomly oriented prolate spheroids with aspect ratio 2 and effective volume-equivalent-sphere size parameter 10. The relative refractive index is 1.5 + i0.005 and the size distribution is given by Eq. (5.244) with an effective variance $v_{\rm eff} = 0.2$.

much greater opportunity for multiple scattering among all the spheres forming the cluster and results in stronger differences between the single-sphere and random-orientation-cluster elements of the scattering matrix.

Based on the results for linear chains of spheres, we may expect that scattering patterns for low-density aggregates of wavelength-sized particles look similar to those for bispheres. This is indeed demonstrated by the laboratory data measured by Muñoz *et al.* (2000b, 2001) for a sample of fly ash aerosols (fluffy aggregates composed of nearly spherical inorganic particles; see Fig. 10.62). Figure 10.63 shows that the normalized scattering matrix for this sample is distinctly different from the average scattering matrix for compact irregular particles derived by Volten *et al.* (2001) (see Section 10.7). Moreover, the experimental results depicted in Fig. 10.63 appear to be remarkably similar to the results of theoretical computations displayed in Fig. 10.59. In particular, the phase function of fly ash particles has the deep side-scattering minimum typical of single spheres and bispheres, the ratios a_3/a_1 and a_4/a_1 tend to values close to –1 as the scattering angle approaches 180°, and the ratio a_2/a_1 is closer to unity than that for compact nonspherical particles. Also, the ratios $-b_1/a_1$ and b_2/a_1 for fly ash and compact irregular particles are qualitatively similar to those computed for polydisperse bispheres and spheroids, respectively.

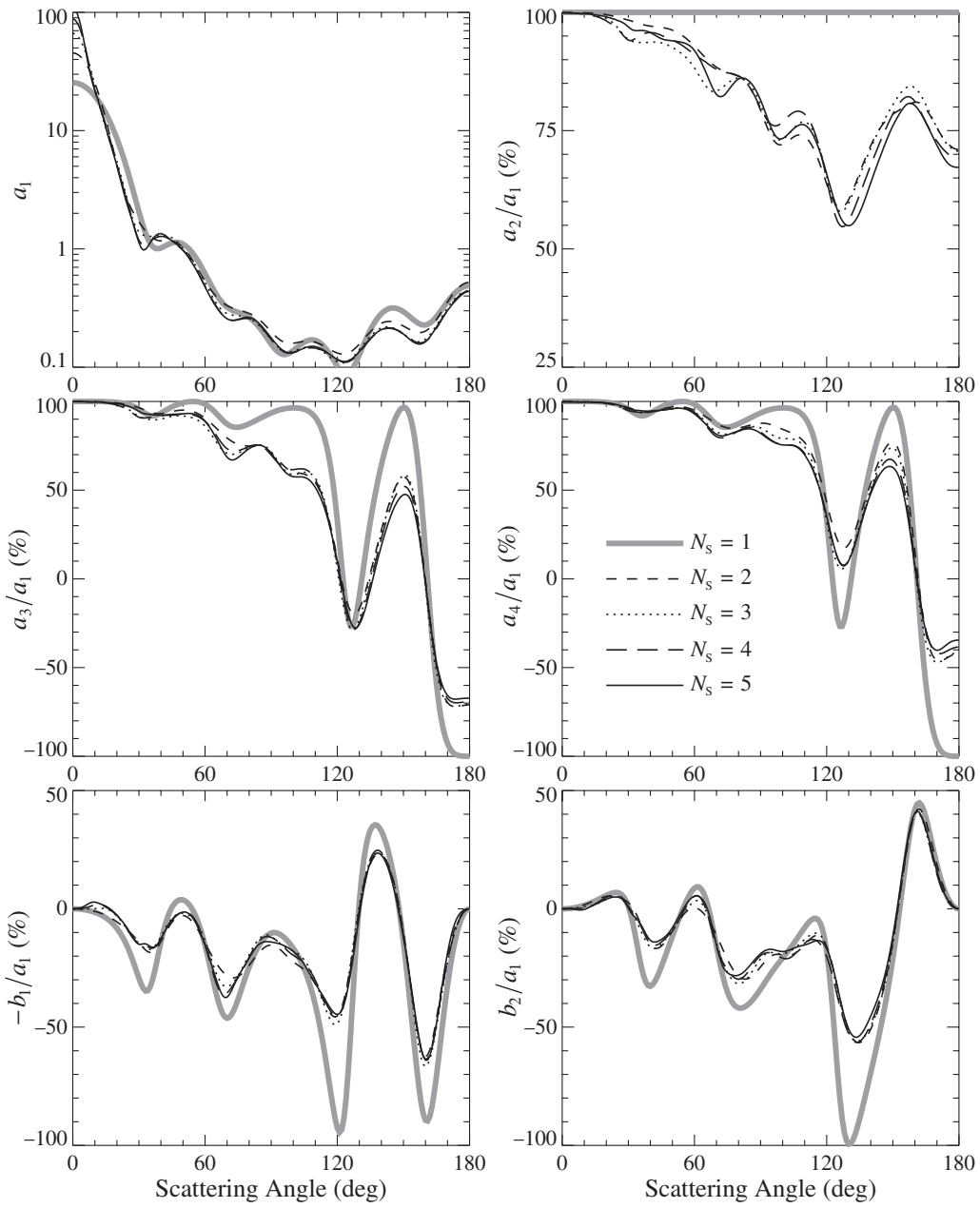

Figure 10.60. Orientation-averaged scattering matrix elements for linear chains of N_s equal spheres. The component-sphere size parameter is 5 and the relative refractive index is 1.5 + i0.005. (After Mackowski and Mishchenko 1996.)

Since clusters of small monomers are abundant in various natural and artificial environments, cluster optics is an important and active area of research. Detailed information and further references can be found in the reviews by Fuller and Mackowski (2000) and Sorensen (2001) and the book edited by Markel and George (2001).

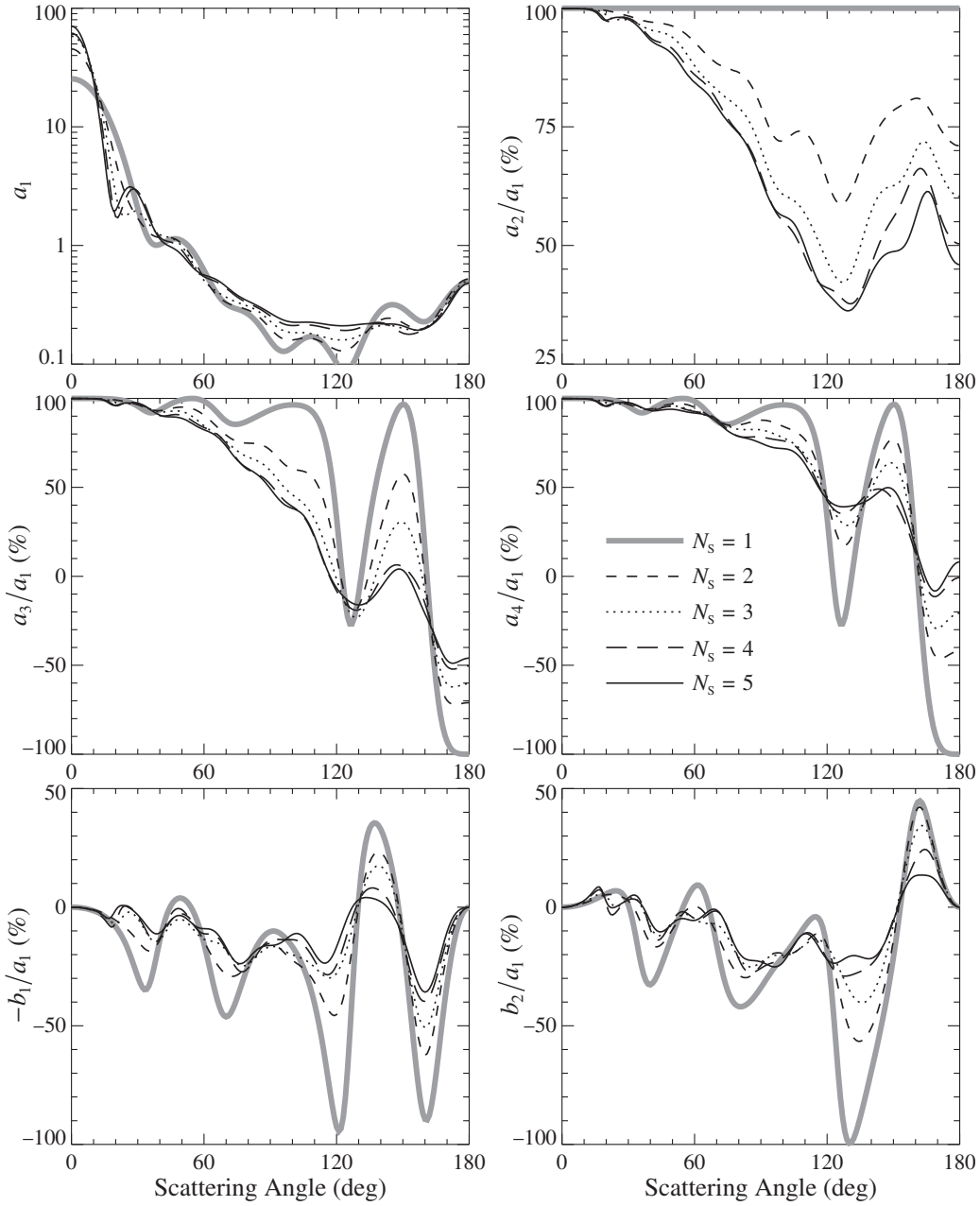

Figure 10.61. As in Fig. 10.60, but for packed clusters of N_s equal spheres. (After Mackowski and Mishchenko 1996.)

10.10 Particles with multiple inclusions

Another interesting class of scatterers are particles with multiple randomly positioned inclusions. Typical examples are water droplets and sulfate aerosols in the terrestrial atmosphere that contain various insoluble impurities (Chýlek *et al.* 1995, 1996), ice particles with internally trapped air bubbles and mineral and soot inclusions (Macke

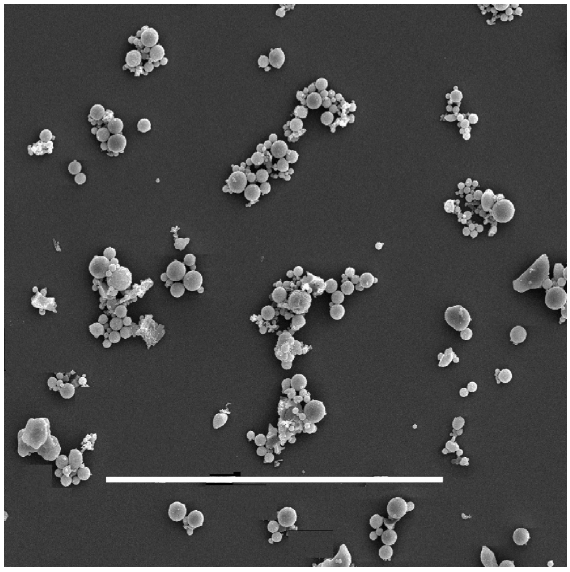

Figure 10.62. Scanning electron microscope photograph of inorganic fly ash particles produced by the combustion of powdered coal in electric powerplants. The length of the white bar corresponds to 100 μm. (From Muñoz *et al.* 2000b.)

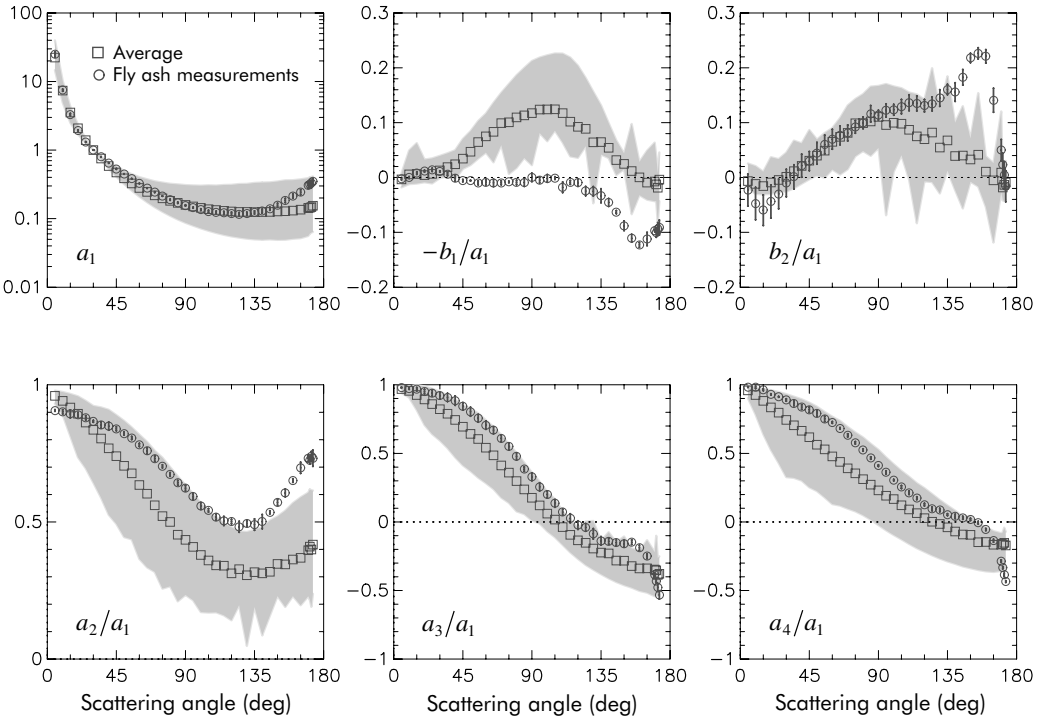

Figure 10.63. The circles depict the measurements by Muñoz *et al.* (2000b) for fly ash particles at a wavelength 633 nm. The squares show the average scattering matrix derived by Volten *et al.* (2001) using measurements for seven samples of compact mineral particles, while the gray bands indicate the domains of sample variability. The sign of the ratio b_2/a_1 is opposite to that adopted elsewhere in this book.

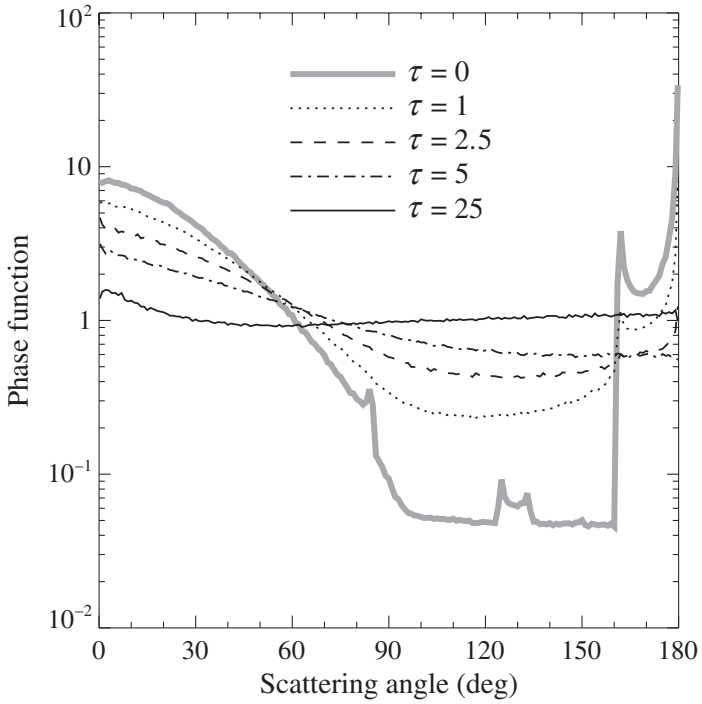

Figure 10.64. The ray-tracing part of the phase function versus scattering angle for a 50-μm-diameter spherical particle containing type-1 inclusions. The optical thickness of the inclusions increases from $\tau = 0$ (no inclusions) to $\tau = 25$ (after Mishchenko and Macke 1997).

et al. 1996a; C.-Labonnote *et al.* 2001), and inhomogeneous composites of mineral particles.

Light scattering by wavelength-sized spheres with a few inclusions can be computed using the superposition *T*-matrix method (cf. Section 5.9). When the host particle is much larger than the wavelength of the incident light, the only feasible approach is the Monte Carlo ray-tracing procedure described in Section 7.4. Figures 10.64 and 10.65 show the ray-tracing part of the phase function for a large spherical host particle with two types of small inclusions. The host has diameter $D = 50\,\mu\text{m}$ and refractive index relative to vacuum 1.55. The latter is a value typical of the real part of the refractive index of silicate materials. The inclusions are modeled as a gamma distribution, Eq (5.245), of spherical particles, with effective radius $0.5\,\mu\text{m}$ and effective variance 0.1. The refractive indices of the inclusions relative to vacuum are 1 (type 1, shown in Fig. 10.64) and 2 (type 2, Fig. 10.65). Type-1 inclusions represent small voids inside the host particle, whereas type-2 inclusions correspond to highly refractive impurities. The vacuum wavelength of the light is fixed at $0.55\,\mu\text{m}$. The overall scattering and absorption effect of the inclusions depends on their "optical thickness" $\tau = n_0 D\langle C_{\text{ext}}\rangle$, where n_0 is the inclusion number density and $\langle C_{\text{ext}}\rangle$ the average extinction cross section per inclusion. For reference, the total numbers of type-1 and type-2 inclusions inside the 50-μm-diameter spherical host corresponding to $\tau = 25$ are 29 469 and 18 967, respectively.

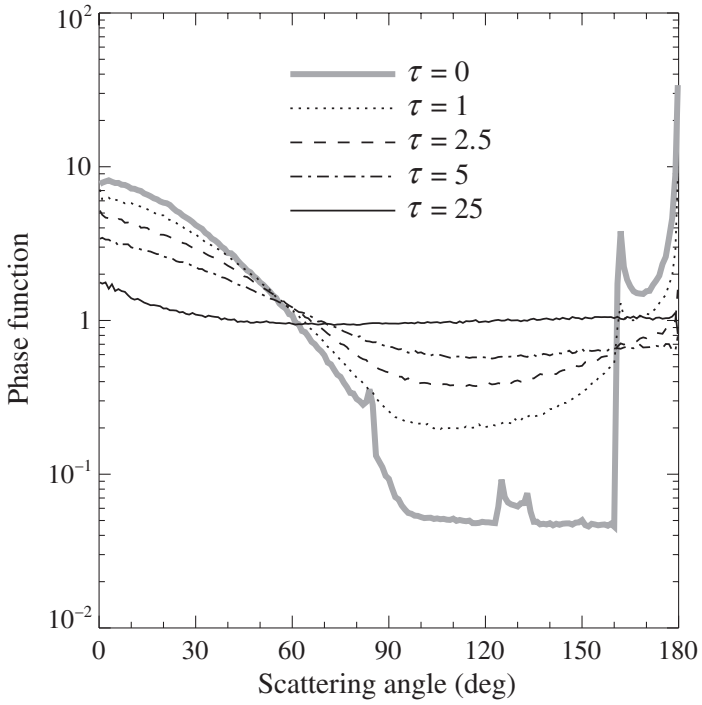

Figure 10.65. As in Fig. 10.64, but for type-2 inclusions (after Mishchenko and Macke 1997).

Figures 10.64 and 10.65 show that the ray-tracing phase function for a clear host (i.e., one having no inclusions) exhibits the pronounced geometrical optics features that are typical of large spherical particles and are discussed in detail in Section 9.4. With increasing τ, these features rapidly weaken and the ray-tracing phase functions become more and more isotropic, in qualitative agreement with the results of laboratory measurements by McGuire and Hapke (1995). Similarly, the effect of inclusions on the phase function of hexagonal ice crystals is to wash out the primary and secondary halos and the backscattering peak (Macke *et al.* 1996a). These effects can be explained qualitatively by increased multiple scattering among the inclusions, which tends to randomize the directions of rays exiting the host. Accordingly, the total asymmetry parameter of the composite spherical particles decreases from approximately 0.815 for $\tau = 0$ to approximately 0.5 for $\tau = 25$ (Fig. 10.66).

When the size of the inclusions is much smaller than the wavelength, a widely used approach is to assume that the composite particle is homogeneous and has an "effective" permittivity obtained by combining in a certain way the permittivities of the host and the inclusions. Several effective-medium approximations and their ranges of applicability are reviewed by Sihvola (1999) and Chýlek *et al.* (2000).

10.11 Optical characterization of nonspherical particles

There are two basic reasons why the optical characterization of nonspherical particles is significantly more involved than that of spherical particles. First, solving the direct

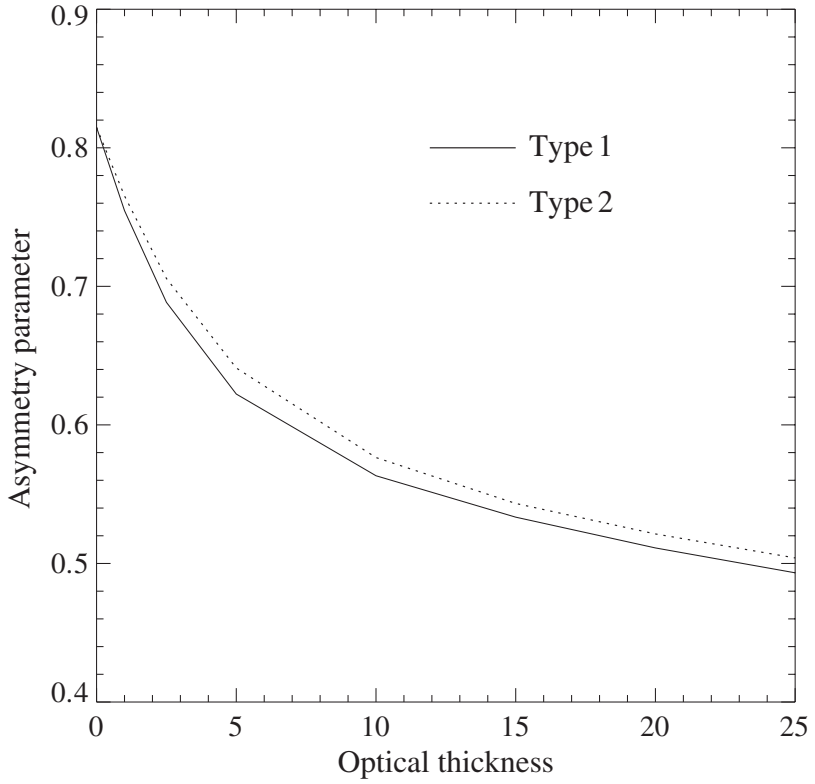

Figure 10.66. Total asymmetry parameter for 50-μm-diameter composite spherical particles containing type-1 and type-2 inclusions, with optical thickness varying from $\tau = 0$ (no inclusions) to $\tau = 25$ (after Mishchenko and Macke 1997).

scattering problem for nonspherical particles is more difficult than applying the standard Lorenz–Mie theory for spheres. Second, solving the inverse problem requires the introduction of at least two (and often many more) additional model parameters describing the particle shape and the orientation distribution function. These additional parameters are often unknown and must be retrieved from the experimental data, along with the particle size and the relative refractive index.

Apparently the simplest task is the detection of preferentially oriented nonspherical particles using the qualitative criteria summarized in Section 4.9. We have already mentioned in this regard observations of interstellar polarization and measurements of the depolarization of radio waves propagating through falling hydrometeors. Another technique involves directing the incident unpolarized beam along the *z*-axis of the laboratory reference frame and measuring the two-dimensional angular distribution of the scattered intensity. The lack of axial symmetry in this distribution will be an unequivocal indication of the presence of oriented nonspherical particles (see Figs. 10.1–10.5 and Section 10.1). This technique will fail, however, when axially symmetric particles are present whose rotation axes are also directed along the *z*-axis (note the upper left panels of Figs. 10.2–10.5). Also, it may be difficult to use such

measurements to say something specific about the particle microphysical characteristics. We have seen in Section 10.1 that the number of patches per unit solid angle in the scattering diagram may be indicative of the particle size parameter, while features such as the bright vertical bands in the upper right panels of Figs. 10.3 and 10.5 may suggest the presence of cylindrical particles with axes perpendicular to the scattering plane. However, more research is obviously needed in order to realize fully the potential information content of two-dimensional scattering measurements (e.g., Sachweh *et al.* 1995; Barthel *et al.* 1998; Dick *et al.* 1998; Kaye 1998; Braun and Krieger 2001; Crosta *et al.* 2001; Prabhu *et al.* 2001; Secker *et al.* 2001).

An interesting laboratory technique for detecting nonspherical aerosols is to subject the particles in question to a pulsed external electric field and look for accompanying changes in the particle optical properties (Kapustin *et al.* 1975, 1980). The amplitude of the field is chosen to be sufficient to cause a significant degree of particle alignment provided that the aerosols are nonspherical, while the duration of the pulse is long enough to allow an equilibrium orientation to be reached. After the electric field is turned off, the particles return to random orientation, owing to Brownian motion. Any differences in the elements of the phase and extinction matrices or the total optical cross sections between the states with the electric field turned on and off indicate the presence of nonspherical particles. Furthermore, the magnitude of the differences and the relaxation time for the disorientation process after the electric field is turned off may indicate a value for the average particle aspect ratio.

As we have seen previously (cf. Section 4.9), the only unequivocal indicator of nonsphericity for randomly oriented particles forming a macroscopically isotropic and mirror-symmetric medium is violation of the Lorenz–Mie identities $F_{22}(\Theta) \equiv F_{11}(\Theta)$ and $F_{44}(\Theta) \equiv F_{33}(\Theta)$. As a consequence, the linear and circular backscattering depolarization ratios defined by Eqs. (10.2) and (10.3) become non-zero. Backscattering depolarization measurements are widely used for detecting and characterizing nonspherical particles in lidar (Gobbi 1998; Sassen 2000) and radar (Aydin 2000; Bringi and Chandrasekar 2001) atmospheric remote sensing and biomedicine (Schmitt and Xiang 1998; de Boer *et al.* 1999). For example, Liu and Chandrasekar (2000) and Straka *et al.* (2000) reviewed the foundation of fuzzy logic systems for classification of hydrometeor type based on polarimetric radar observations. Sassen (1991) developed a depolarization classification of different cloud-particle types based on data collected by a helium–neon continuous-wave laser-lidar analog device in the laboratory and field during the early 1970s (Fig. 10.67). Browell *et al.* (1990) used lidar depolarization observations to differentiate between various types of polar stratospheric clouds. Although most lidars operating at visible wavelengths measure the linear depolarization ratio, measurements of the circular depolarization ratio are also gaining popularity (Woodard *et al.* 1998).

The strong depolarization of light by large transparent particles such as ice cloud crystals at visible wavelengths (Fig. 10.67) is traditionally attributed to refractions and multiple internal reflections (Fig. 7.2), which tend to randomize the polarization

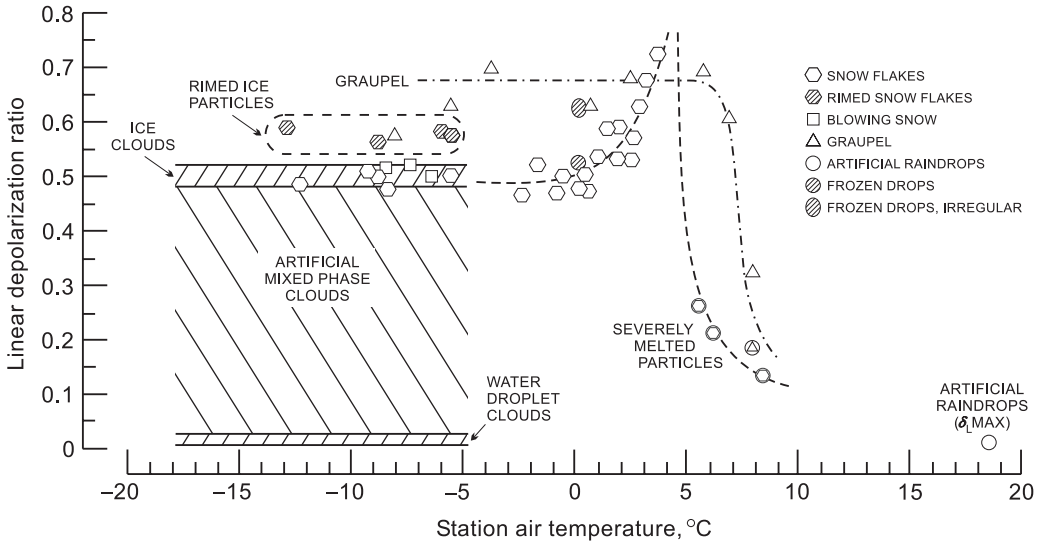

Figure 10.67. Results of early laboratory and field studies showing the wide range of linear depolarization ratios encountered from various types of hydrometeors at visible wavelengths (from Sassen 1991).

plane of rays exiting the particle (Liou and Lahore 1974). However, the geometrical optics concepts of rays, refractions, and reflections become inapplicable when the size of the particle is comparable to the wavelength. Yet wavelength-sized particles can produce even larger depolarization ratios, as demonstrated in Fig. 10.68. An interesting feature of essentially all the depolarization curves shown in this figure and computed with the exact *T*-matrix method is a rapid increase in δ_L as the effective size parameter increases from 0 to about 10. Moreover, maximal δ_L-values for most shapes are observed at size parameters close to and sometimes slightly smaller than 10. The *T*-matrix results show no obvious relationship between δ_L and the particle aspect ratio. Even spheroids with aspect ratio as small as 1.05 (a 2.5% deviation from the perfect spherical shape) produce strong depolarization. The largest δ_L-values are generated by prolate spheroids with aspect ratios as small as 1.2 (a 10% deviation from a sphere). Furthermore, δ_L for spheroids and, especially, cylinders tends to saturate with increasing aspect ratio.

The steep rise in δ_L with size parameter in the range $0 \lesssim x_{\text{eff}} \lesssim 10$ exhibited by the *T*-matrix results can explain the initial increase in lidar linear depolarization with time for very young, rapidly growing aircraft condensation-trail (contrail) particles observed by Freudenthaler *et al.* (1996). Figure 10.68 suggests that further growth of ice particles may lead to a decrease in δ_L with time, which was indeed observed by Sassen and Hsueh (1998). Furthermore, the *T*-matrix results seem to explain the occurrence of unusually large depolarization ratios for contrails ($\delta_L \sim 0.65$), which exceed significantly the values normal for most cirrus ($\delta_L \sim 0.35$–0.5). Similar *T*-matrix computations have been used by Carslaw *et al.* (1998), Toon *et al.* (2000), Beyerle *et al.* (2001), and Liu and Mishchenko (2001) to explain the results of lidar

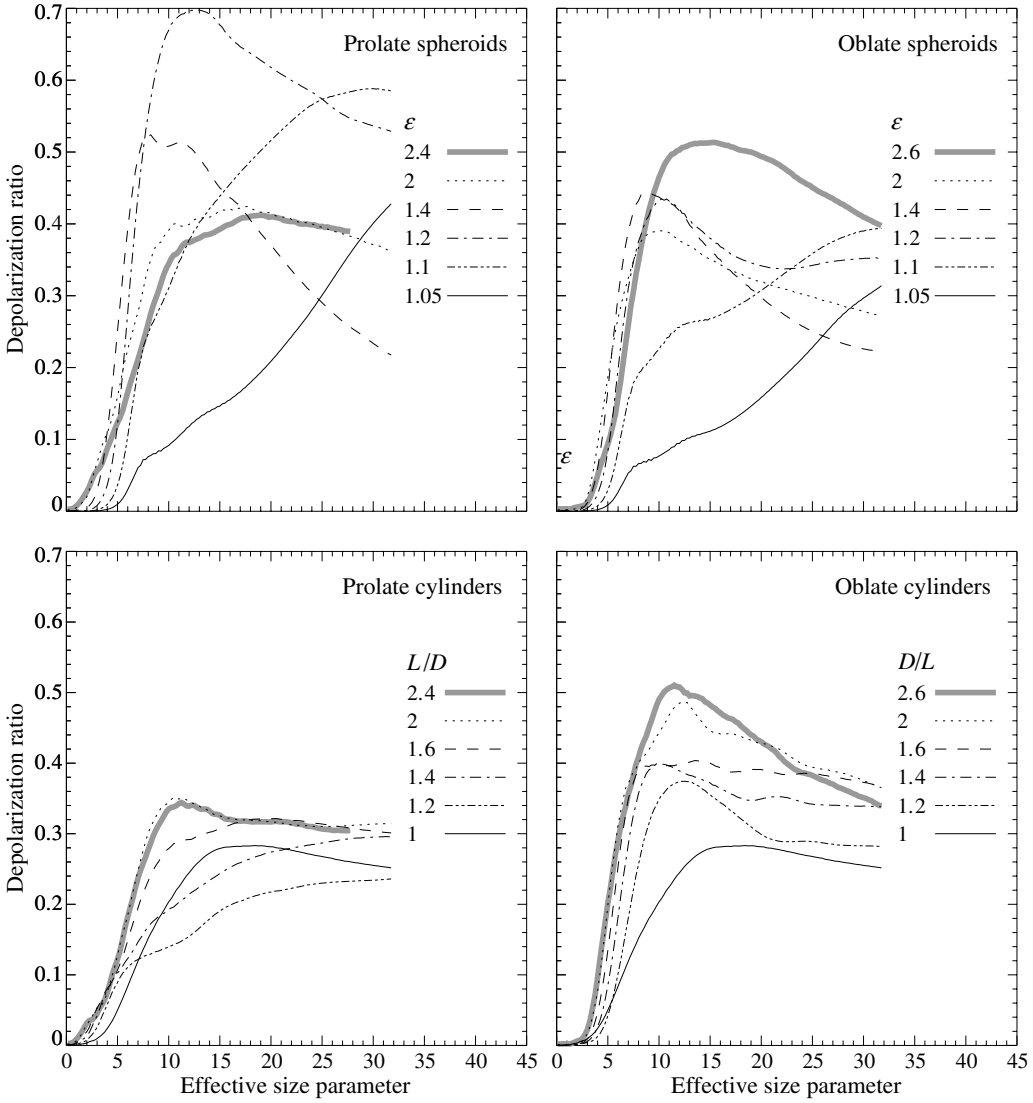

Figure 10.68. Linear backscattering depolarization ratio versus effective size parameter for polydisperse, randomly oriented ice spheroids with aspect ratios ranging from 1.05 to 2.6 and circular cylinders with various length-to-diameter or diameter-to-length ratios. The relative refractive index is 1.311 and the size distribution is given by Eq. (5.246) with $\alpha = -3$ and $v_{\text{eff}} = 0.1$. (After Mishchenko and Sassen 1998.)

observations of polar stratospheric cloud particles, which are another interesting example of natural wavelength-sized scatterers generating strong depolarization ratios.

In view of the apparent strong dependence of depolarization on size parameter for wavelength-sized particles, measuring depolarization at multiple wavelengths should be very useful for retrieving particle size and studying its temporal evolution. As an example, Plate 10.9 shows a variety of remote sensing observations of a mesoscale cirrus cloud band with contrails along its edges performed by Sassen *et al.* (2001) on 5 March 1999. It can be seen from the fish-eye images and the depolarization

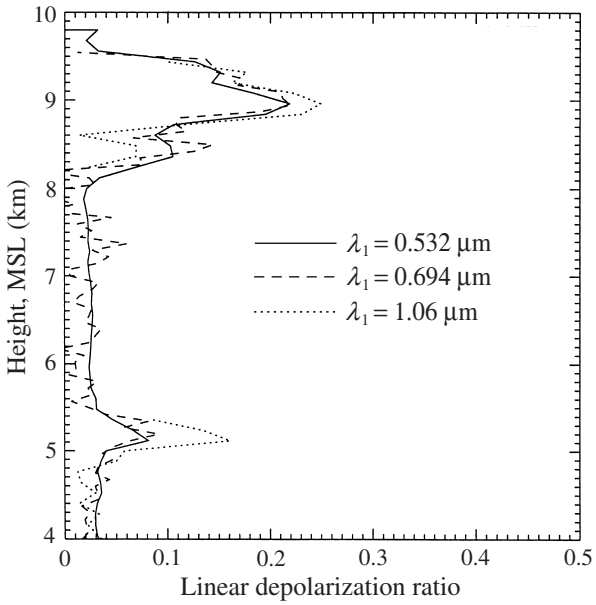

Figure 10.69. Comparison of 5-minute-averaged (1854–1859 UTC) linear depolarization profiles for three lidar wavelengths during a period when the backscattered intensity from the elevated aerosol layer was relatively strong. Table 10.5 gives the depolarization values at the ~5.25 km aerosol maximum in terms of the total molecular and aerosol and aerosol-only values. (From Sassen *et al.* 2001.)

displays that the contrails occurred just above the cirrus cloud top at the very beginning (missing the contrail leading edge) and at the end of the measurement period, when two contrails passed overhead in succession. Although the backscattered intensity displays at the $0.532\,\mu m$ (bottom left panel) and $1.06\,\mu m$ (bottom right) wavelengths are similar, there are large differences between the respective depolarization displays. The significantly smaller δ_L-values in the contrail at the longer wavelength imply the presence of $\sim 2\,\mu m$ diameter crystals (cf. Fig. 10.68), despite the fact that the contrails were probably of order one hour old when observed in the zenith. In contrast, the δ_L-values in the main cirrus cloud at the two wavelengths are quite similar, as can be expected of nonabsorbing particles with sizes much larger than a wavelength. It can, therefore, be concluded that contrails are unique among ice clouds in their ability to generate and maintain sufficiently tiny ice-particle sizes to manifest the depolarization dependence typical of the transition zone between the Rayleigh and the geometrical optics region of size parameters.

Another interesting feature of the lidar displays in Plate 10.9 is the significant depolarization caused by the elevated aerosol layer centered at about 5.3 km. This aerosol was almost certainly a product of the transport of dust from Asian dust storms. As more clearly seen in Fig. 10.69, the δ_L-values at the three lidar wavelengths reveal differences which may be attributed partly to significant noise in the weak aerosol backscattering and partly to the decreasing contribution of weakly depolarizing

Table 10.5. Linear depolarization ratio at the ~ 5.25 km aerosol maximum in terms of the total molecular and aerosol (δ_{L}) and aerosol-only ($\delta_{\mathrm{L,a}}$) values at the three lidar wavelengths (after Sassen *et al*. 2001)

λ_{I} (μm)	δ_{L}	$\delta_{\mathrm{L,a}}$
0.532	0.08	0.21
0.694	0.09	0.23
1.06	0.16	0.25

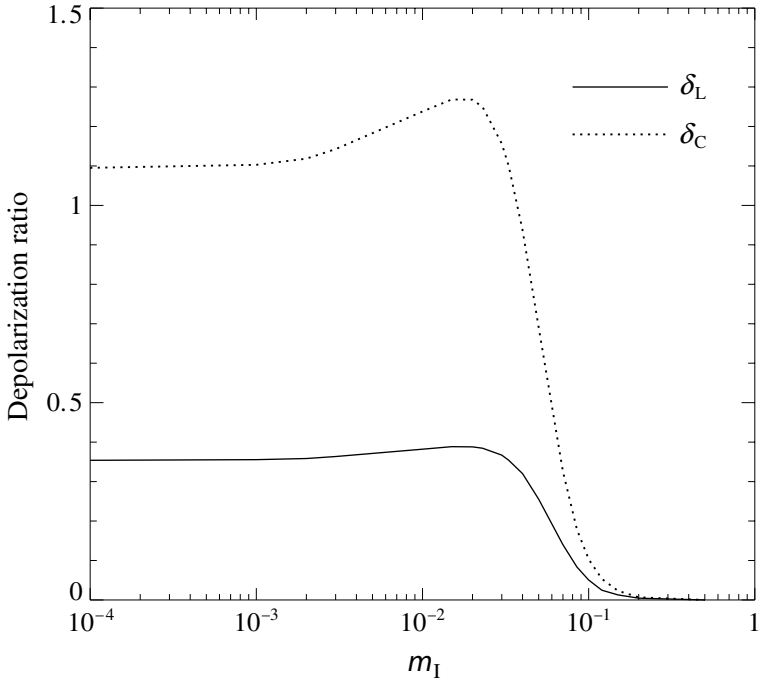

Figure 10.70. Linear and circular backscattering depolarization ratios versus imaginary part of the relative refractive index for polydisperse, randomly oriented oblate spheroids with $a/b = 1.7$. The size distribution is given by Eq. (5.246) with $\alpha = -3$ and $v_{\mathrm{eff}} = 0.1$. The effective surface-equivalent-sphere size parameter is $x_{\mathrm{eff}} = 15$ and the real part of the relative refractive index is 1.31.

molecular scattering to the total molecular plus aerosol depolarization with increasing wavelength (cf. Eq. (7.6), which indicates that the molecular contribution to the total molecular plus aerosol scattering matrix decreases as the inverse fourth power of wavelength). Table 10.5 shows that when the molecular backscattering contributions are approximately removed, the aerosol-only peak depolarization values are about 0.2–0.25, which is similar to the strong Kosa dust-dominated depolarization measured in Japan (Murayama *et al.* 1999; Sassen 2000). The spectral effect of molecular scattering on the total molecular plus cloud depolarization, the feature at about 9 km

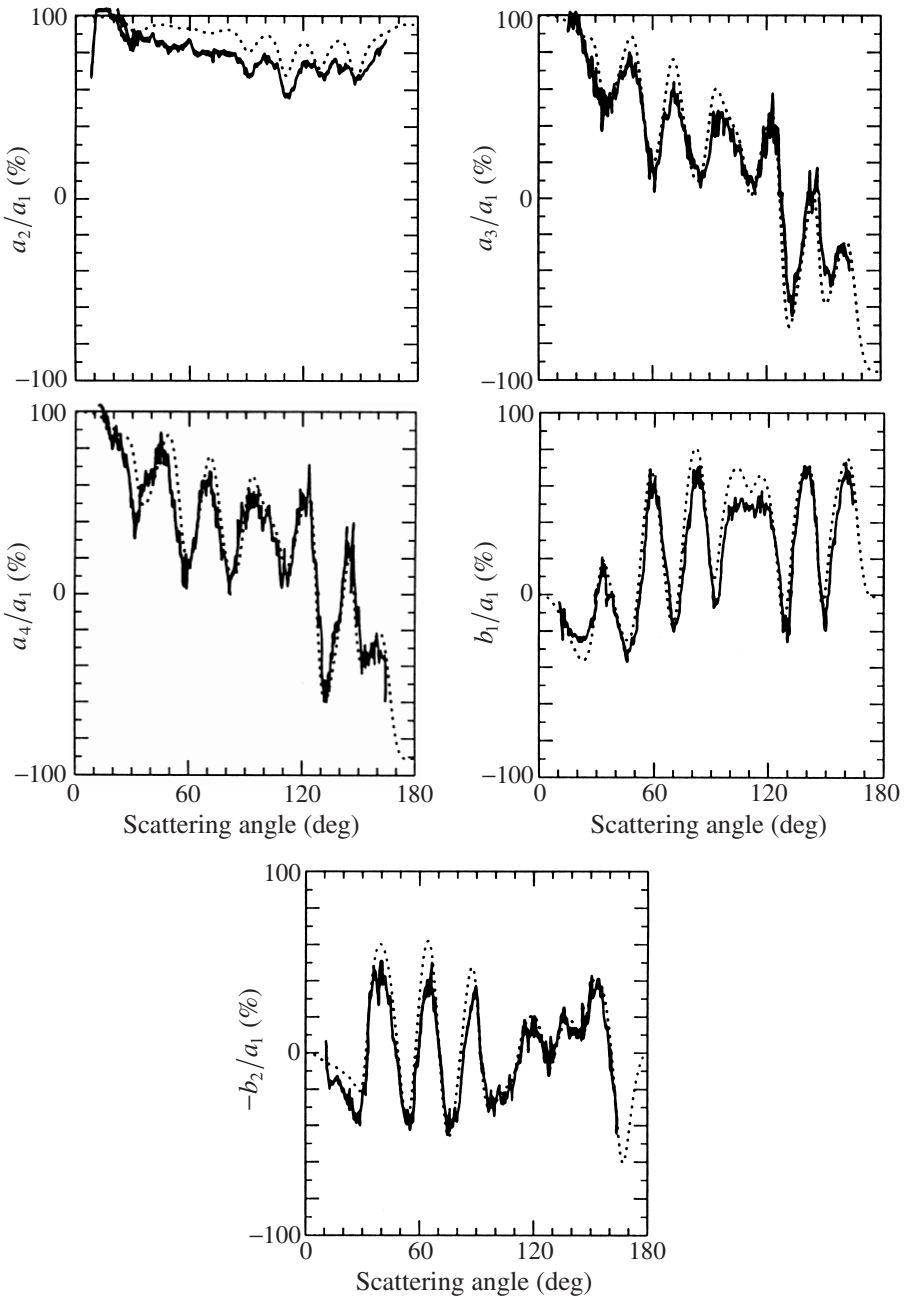

Figure 10.71. Ratios of the elements of the normalized Stokes scattering matrix for a latex two-sphere cluster in random orientation. The solid curves depict laboratory data of Bottiger *et al.* (1980) at a wavelength 441.6 nm, whereas the dotted curves show the results of *T*-matrix computations for a component-sphere diameter 1129 nm.

in Fig. 10.69, is significantly weaker because of the much stronger cloud backscattering.

We saw in Section 10.2 that increasing imaginary part of the relative refractive index m_I reduces and eventually eliminates the differences between the scattering pat-

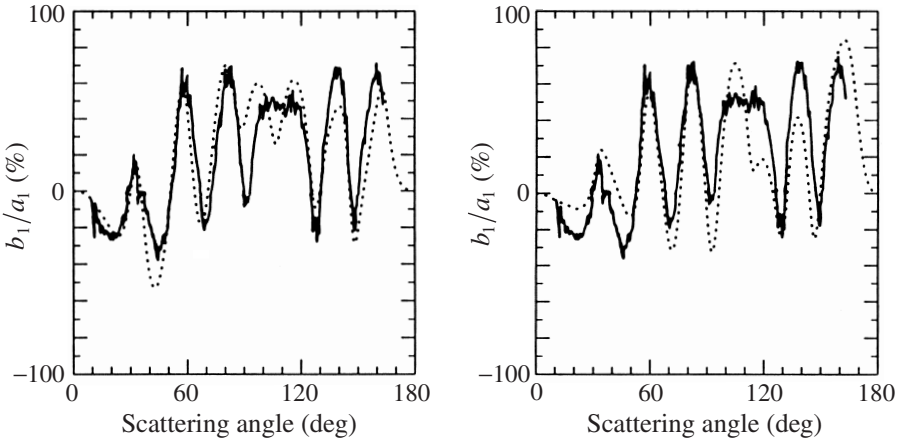

Figure 10.72. As in Fig. 10.71, but for component-sphere diameters 1108 nm (left-hand panel) and 1150 nm (right-hand panel).

terns of spherical and surface-equivalent convex nonspherical particles. Accordingly, increasing m_I leads to reduced and ultimately zero linear and circular depolarization ratios, as Fig. 10.70 illustrates. This factor limits the usefulness of depolarization observations of cirrus clouds and contrails at infrared wavelengths (Eberhard 1992), where water ice is strongly absorbing (Warren 1984).

A more detailed characterization of randomly oriented nonspherical particles can be achieved by exploiting multi-angle measurements of the full scattering matrix (e.g., Volten *et al.* 1999). The results can be especially precise when one or more particle microphysical parameters are known beforehand. As an example, Figs. 10.71 and 10.72 parallel Figs. 9.30 and 9.31 in showing the results of laboratory measurements (Bottiger *et al.* 1980) and *T*-matrix computations (Mishchenko and Mackowski 1996) for a two-sphere cluster with touching components. An electrostatically levitated latex bisphere was subject to Brownian motion and rapidly changed its orientation during the measurement. Therefore, although the sample was a single particle, the measurement of the scattering matrix was equivalent to that for randomly oriented monodisperse particles. According to Bottiger *et al.*, this was indeed corroborated by simultaneous measurements of the (1,3), (1,4), (2,3), (2,4), (3,1), (3,2), (4,1), and (4,2) elements of the scattering matrix, which were all found to be zero within the experimental accuracy (cf. Eq. (4.51)). Since the particle morphology and relative refractive index are known, the only free parameters are the diameters of the component spheres. Mishchenko and Mackowski have found that good agreement between the results of *T*-matrix computations and laboratory measurements can be obtained for component sphere diameters equal to 1129 nm (Fig. 10.71). Figure 10.72 shows the results for sphere diameters 1108 nm and 1150 nm, which give limits on the plausible range of diameters. This illustrates once again the potential accuracy of particle sizing techniques based on measurements of the scattering matrix.

Further reading

The book edited by Mishchenko *et al.* (2000a) is a major systematic source of information on calculations, measurements, and applications of electromagnetic scattering by nonspherical and heterogeneous particles. Further information can be found in the special journal issues edited by Shafai (1991), Barber *et al.* (1994), Hovenier (1996), Lumme (1998), Mishchenko *et al.* (1999a,b), and Videen *et al.* (2001) and in the conference proceedings edited by Schuerman (1980), Wriedt *et al.* (1996), Wriedt and Eremin (1998), Obelleiro *et al.* (1999), and Videen *et al.* (2000b). The book by Colton and Kress (1998) treats mathematical and numerical aspects of the inverse scattering problem for electromagnetic and acoustic waves.

Scattering by randomly and preferentially oriented spheroids and finite circular cylinders in the geometrical optics limit is discussed by Yang and Cai (1991), Arnott and Marston (1991), Macke and Mishchenko (1996), Kokhanovsky and Nakajima (1998), Langley and Marston (1998), and Marston (1999). Listed in Sassen and Arnott (1998) are several feature journal issues discussing optical phenomena associated with natural ice crystals.

Appendix A

Spherical wave expansion of a plane wave in the far-field zone

In this appendix we derive Eq. (2.57) following the approach described by Saxon (1955b). We begin with the well-known expansion of a plane wave in scalar spherical harmonics (Jackson 1998, page 471):

$$\exp(\mathrm{i}\mathbf{r}\cdot\mathbf{r}') = 4\pi \sum_{l=0}^{\infty} \mathrm{i}^l j_l(rr') \sum_{m=-l}^{l} Y_{lm}^*(\hat{\mathbf{r}}) Y_{lm}(\hat{\mathbf{r}}'), \tag{A.1}$$

where $\hat{\mathbf{r}} = \dfrac{\mathbf{r}}{r}$, $\hat{\mathbf{r}}' = \dfrac{\mathbf{r}'}{r'}$, the $j_l(y) = y^l \left(-\dfrac{1}{y}\dfrac{\mathrm{d}}{\mathrm{d}y} \right)^l \left(\dfrac{\sin y}{y} \right)$ are spherical Bessel functions of the first kind, and the $Y_{lm}(\hat{\mathbf{r}})$ are scalar spherical harmonics. The latter are defined as

$$Y_{lm}(\hat{\mathbf{r}}) = \sqrt{\frac{(2l+1)(l-m)!}{4\pi(l+m)!}}\, P_l^m(\cos\vartheta)\mathrm{e}^{\mathrm{i}m\varphi}, \tag{A.2}$$

where ϑ and φ are spherical angular coordinates of the unit vector $\hat{\mathbf{r}}$ and P_l^m are associated Legendre functions defined in terms of Legendre polynomials P_l as follows:

$$P_l^m(x) = (-1)^m (1-x^2)^{m/2} \frac{\mathrm{d}^m}{\mathrm{d}x^m} P_l(x), \quad P_l(x) = \frac{1}{2^l l!} \frac{\mathrm{d}^l}{\mathrm{d}x^l} (x^2-1)^l \tag{A.3}$$

with $x \in [-1, 1]$. Using the asymptotic form (Arfken and Weber 1995, p. 682)

$$j_l(y) \underset{y\to\infty}{=} \frac{1}{y} \sin\left(y - \frac{\pi l}{2} \right), \tag{A.4}$$